UNIVERSITY OF CAPE TOWN
DEPARTMENT OF PHYSICS

NEUTRON SPECTRUM FROM ^{252}Cf SPONTANEOUS FISSION

M.S. ALLIE

Thesis submitted in partial fulfilment of
the requirements for the degree of

MASTER OF SCIENCE

in the Faculty of Science
May 1984

ABSTRACT

Measurements have been made of the neutron spectrum from the spontaneous fission of ^{252}Cf in the restframe of the fragment by simultaneous observation of the neutron time-of-flight and the fragment velocity. The fragments were detected by means of thin film plastic scintillators in which the scintillation pulse-height response was verified to be a linear function of fragment velocity. The measurements of the neutron spectrum in the restframe of the fragment are compared with previous work and are found to deviate significantly from the predicted observations of the simple form of the evaporation model.

Acknowledgements

I express my appreciation and gratitude to :

Professor F.D. Brooks, my supervisor, for his help and guidance throughout the project and for his encouraging advice on the compilation of this thesis;

Dr. W.A. Cilliers who was constantly involved with the work especially the development of the thin film plastic scintillators;

Dr. H.S.T. Driver for his help with measuring the thicknesses of the thin plastic foils;

The scientific and technical staff of the Southern Universities Nuclear Institute for assistance with the experimental work;

The Staff of the Computing Services Centre of UCT;

Fellow students Bruce Simpson and Ricky Smit who assisted with some of the computing and experimental work;

Mr Piet Groenewald for drawing most of the diagrams;

Sue Allen, Shanaaz Hassiem and Faiza Toefy for typing and checking various parts of the manuscript;

Ginny Blewett for typing the figure captions and making overall corrections to the manuscript;

My parents for their support and encouragement of my studies.

Table of contents

4. CHAPTER FOUR: RESULTS AND DISCUSSION

1. CHAPTER ONE: OVERVIEW

1.1. Introduction

Since the discovery of nuclear fission by Hahn and Strassman (Ha39) in 1939 and the subsequent interpretation of this cataclysmic phenomenon by Frisch and Meitner (Fr39a), a large effort both experimentally and theoretically has been made in order to gain a full understanding of this aspect of nuclear physics. At present, however, there is still no single theory that can account satisfactorily for all the experimental observations. The first comprehensive theoretical treatment was that proposed by Bohr and Wheeler (Bo39) in which the analogy between the splitting of a liquid drop and that of the nucleus was exploited. This liquid-drop model (LDM) used to describe fission is still the most widely used description although many refinements have been incorporated since its inception. A similar model was developed independently by Frenkel (Fr39b). Spontaneous fission was first identified by Pertzhak and Flerov in 1940 (Pe40).

1.2. The liquid-drop model

In the LDM the nucleus is represented by a uniformly charged drop of incompressible nuclear matter enclosed in a well defined surface containing a constant volume. The internal nuclear structure is ignored and the "fission barrier" arises as a result of the difference between the surface tension and the Coulomb repulsion. Various attempts to incorporate the effects of structure in the nucleus have been made, e.g. Swiatecki (Sw55) treated the effect as a shell energy correction to the LDM energy while Strutinsky modulated the LDM potential energy by shell energy corrections which have a quasi- periodical variation as a function of deformation, resulting in "Strutinsky's prescription" for calculating barrier heights (St67, St68). Fission can be divided into two types as regards the pre-fission phase, viz. particle induced fission such as the fission of uranium-235 by thermally induced neutrons, ^{235}U (n_{th},f), and spontaneous fission in which the nucleus decays spontaneously into two or more fragments as in the case of californium-252, ^{252}Cf (sf). Binary fission, in which the nucleus fragments into two portions of roughly equal size, is the most common mode and can be described as the succession of three phases:

(1) The compound nucleus undergoes a long series of collective oscillations until one of them leads to the passing of
(2) the "saddle-point", after which
(3) scission occurs.

One of the striking features of binary fission is that asymmetric mass division is highly favoured. This can be seen in figure 1.1 which shows a plot of the fragment mass distribution for spontaneous fission of californium-252. Although the LDM is a successful model in explaining many of the features of fission it is unable to account for the extremely low probability of symmetric fission.

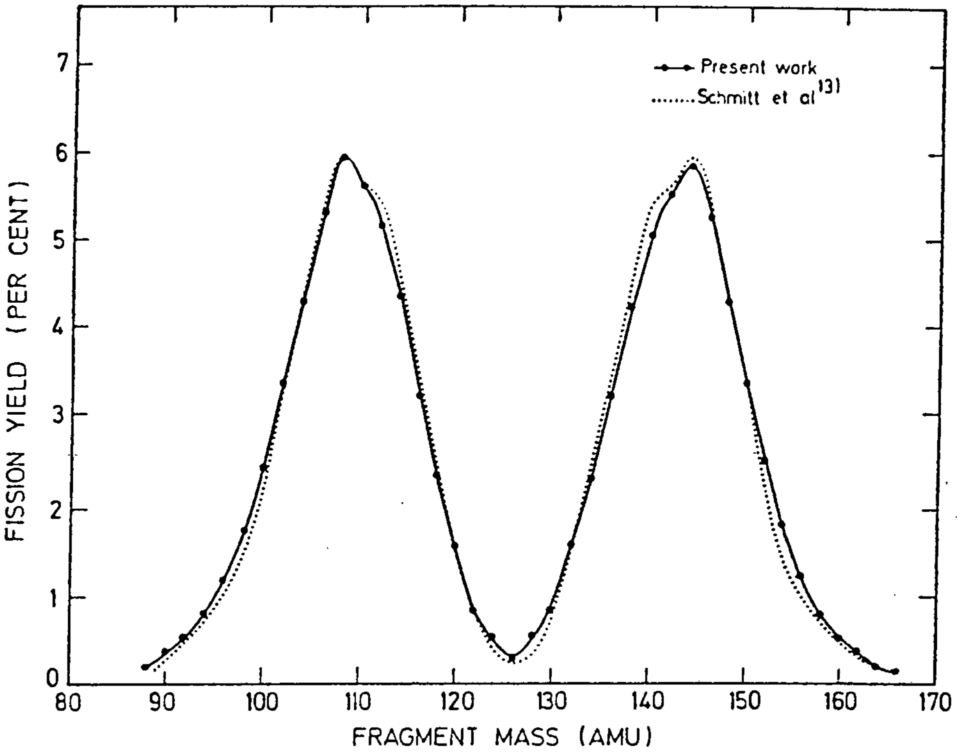

FIGURE 1.1 *The fragment mass distribution for spontaneous fission of ^{252}Cf, showing measurements by Walsh and Boldeman (Wa77), and Schmitt et al (Sc66). (Figure from Wa77).*

Spontaneous fission is a quantum mechanical (tunneling) effect analogous to alpha decay. The wavefunction is, however, that for the motion of a surface going through a potential energy maximum in deformation space. The diagram below, taken from (Hy64), shows such penetration of a fission barrier by a nucleus excited to less than the barrier energy. There is, however, much evidence that this fission barrier has a more complicated shape than is indicated in figure 1.2. A recent review explores the question of the fission barrier in depth (Bj80).

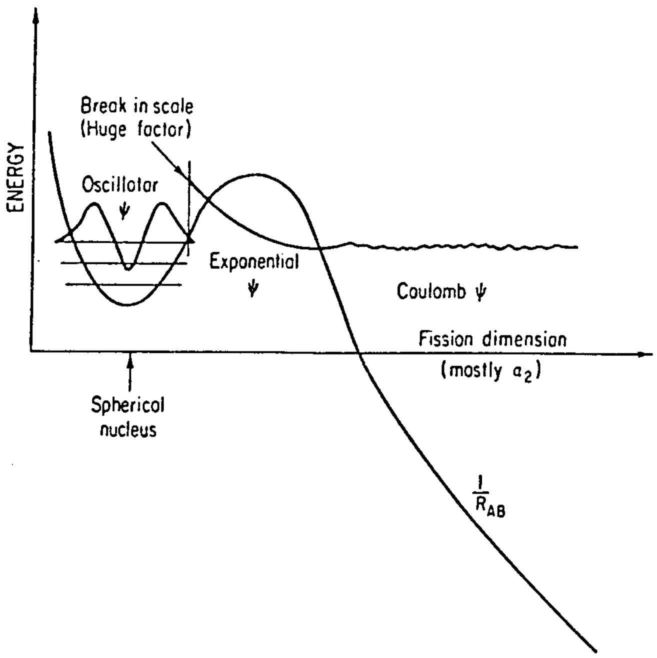

FIGURE 1.2 *Schematic diagram indicating quantum mechanical penetration of a fission barrier by a nucleus excited to less than the barrier energy.*

(Figure from Hyde, (Hy64)).

1.3. Types of particles emitted

It is convenient to group the particles that are emitted during fission as:

(1) particles emitted at the instant of scission,
(2) "prompt" radiations emitted by the moving fragments,
(3) "delayed" radiation.

Should binary fission occur, two fragments are the resultant products at the time of scission. About 1 in every 300 fissions results in two fragments and an alpha particle (Ra68). This relatively rare occurrence is designated ternary fission. At present there is no experimental evidence that any neutrons are are emitted at the time of scission. We discuss the question of scission neutrons in a later paragraph.

The major prompt radiations from the highly excited, neutron-rich fission fragments are neutrons and gamma rays. At least 70% of the total gamma-ray energy is emitted more than one picosecond after fragmentation, while the neutrons are emitted in a time shorter than 10^{-14} seconds (Ni74). About 8 prompt gamma rays occur per fission, dissipating approximately 7 Mev of the fragment excitation energy (Ni74). A percentage of the prompt gamma transitions leads to the emission of electrons and K x-rays via internal conversion (G165 , Th65).

The prompt neutrons, of which, on average, 3.77 (Sp82)are emitted per fission, de-excite the fragment by between 20 and 35 Mev (B063). Figure 1.3 summarises, schematically, the fission process and the relative time scales that are involved in secondary particle emission.

1.4. Prompt neutron spectra

The highly excited fission fragment, considered as a compound nucleus, can also be thought of as a hot surface from which molecules (the neutrons) can escape as in an evaporation process. This way of looking at the decay of the compound nucleus, the evaporation model, was first suggested by Weisskopf in 1937 (We37, B154) and is the most popular model used to predict the shape of the prompt neutron spectrum in the restframe of the fission fragment. As early as 1947, Wilson (Wi47) came to the conclusion that the properties of prompt neutrons were indeed consistent with

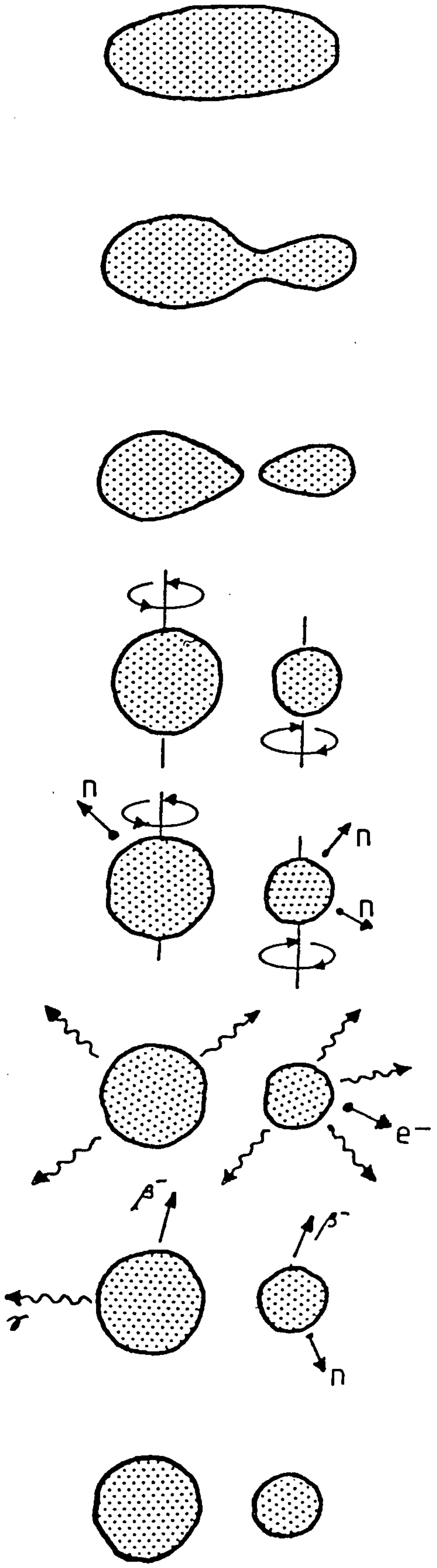

Time scale (seconds)	Scenario
<0	Highly Deformed Nucleus
0	Configuration just before scission
10^{-20}	Scission: Cold, deformed fragments formed. Accelerated by mutual coulomb repulsion
10^{-18}	Fragments: Fully accelerated nearly spherical highly excited
10^{-14}	Neutron evaporation
10^{-10}	Emission of: Cascaded γ-rays x-rays conversion e$^-$
10^{-3} to 10^{2}	Emission of: β^- γ delayed neutrons
	Stable Nuclei

FIGURE 1.3 Schematic diagram of spontaneous fission

evaporation from the moving fragments, while Fraser (Fr52) in confirming this conclusion was also able to set an upper limit of 4×10^{-14} seconds for the time of emission of these neutrons.

The Weisskopf evaporation spectrum may be represented by the equation

$$N(\varepsilon) = \frac{\varepsilon}{T^2} \exp\left(-\frac{\varepsilon}{T}\right) \qquad (1.1)$$

where ε is the centre-of-mass* neutron energy and T is the temperature of the residual nucleus at an excitation energy equal to the difference between the excitation energy of the evaporating nucleus and the neutron separation energy.

One way in which the predictions of the theory may be tested is to transform this spectrum to a spectrum in the laboratory frame. The latter spectrum can then be compared with measurements of the neutron spectrum in this reference frame. However, it has been shown by Terrell (Te59), using results derived earlier by Feather, that the single-valued temperature spectrum (equation 1.1) cannot, however, when transformed to the laboratory frame, account for the observed experimental data. In order to obtain such agreement a

*We note that the terminology "centre-of-mass" as used in the literature on fission refers to one of the two fragment systems after scission has ocurred and not to the fissioning californium system. Since the mass of the evaporating neutron is small in comparison with the fragment from which it is emitted this "centre-of-mass" frame is virtually identical to the restframe of the fission fragment in question.

superposition of evaporation spectra in the fragment restframe at different residual nuclear temperatures is required, i.e.

$$N(\varepsilon) = \sum_i \left(\alpha_i \frac{\varepsilon}{T_i^2}\right) \exp\left(-\frac{\varepsilon}{T_i}\right) \tag{1.2}$$

or, for a continuous range of T,

$$N(\varepsilon) = \int_0^{T_{max}} \left[\alpha(T) \frac{\varepsilon}{T^2}\right] \exp\left(-\frac{\varepsilon}{T}\right) dT \tag{1.3}$$

A fairly substantial body of experimental evidence on both ^{252}Cf (sf) and ^{235}U (n_{th},f) shows that the gross features of the prompt neutron spectrum in the laboratory frame of reference are reasonably well represented by either the Watt (Wa52) or the Maxwellian distributions. The Watt spectrum has the form

$$N(E) = A \exp(-bE) \sinh\sqrt{cE} \tag{1.4}$$

where A is a normalising constant and b and c define the shape. The Watt spectrum arises as the result of assuming a Maxwellian spectrum in the restframe of the fission fragment. This Maxwellian spectrum can be regarded, however, as a special case of the continuous distribution (equation 1.3).

The following form of the Maxwellian spectrum also happens to fit the neutron spectrum in the laboratory frame.

$$N(E) = B \sqrt{E} \exp\left(-\frac{E}{T_m}\right) \tag{1.5}$$

where B is a normalising constant and T_m is related to the average neutron energy by the relation $T_m=\frac{2}{3}\bar{E}$. It should be noted that T_m, which is not the nuclear temperature, is related to the centre-of-mass energy, E_{cm}, by the relation $T=\frac{1}{2}E_{cm}$. Terrell

(Te59) showed the residual nuclear temperature distribution to be approximately triangular in shape. Using superposition of evaporation spectra (equation 1.2) for seven temperatures accordingly, the resulting spectrum, N(E), was shown to be represented by a Maxwellian distribution over the intermediate neutron energy range. However, at both the low and the high neutron energies the Maxwellian spectrum exceeds the values predicted by Terrell.

As has been recently pointed out by Madland and Nix (Ma82), both the Watt and the Maxwellian spectra neglect effects such as

(1)the effect on the fragment residual nuclear temperature distribution by the initial distribution of the fragment excitation energy and the subsequent cooling of the fragment owing to neutron emission and

(2)the energy dependence of the cross-section for the inverse process of compound nucleus formation.

Further, the Maxwellian spectrum neglects the centre-of-mass motion of the fragment from which the neutron is emitted. The result of neglecting the above factors leads to parameters that are adjusted to rather unphysical values in order to reproduce the experimental data. The latest calculations based on standard evaporation theory (Ma82) attempt to take cognisance of these effects.

1.5. Scission neutrons

Bohr and Wheeler (Bo39) and Hill and Wheeler (Hi56) suggested that a component of the prompt neutron spectrum was emitted at the time of scission. This possibility was further investigated theoretically by Fuller (Fu62) and Stavinski (St59). Experimental evidence pointing to the existence of scission-neutrons was reported by Bowman et al (Bo62 and B063) who concluded that only 90% of the prompt neutrons from ^{252}Cf (sf) could reasonably have evaporated from the fully accelerated fragments. They ascribed the remaining 10% to an isotropic component in the laboratory frame arising from the fissioning nuclide at the time of scission. A similar conclusion was reached by Skarsvag and Bergheim (Sk63) for ^{235}U (n_{th},f), their estimate of this component being 15%. However, Terrell (Te65) pointed out that the data are consistent with the emission of 100% of the neutrons from the fragments but with a slight anisotropy at 0° and 180°, citing the work of Sargent et al (Sa65) in support of this view. A further possibility is that the evidence in support of this 'central group' of neutrons might arise as a consequence of insufficiently precise evaluation of the experimental data (Kl71). A re-analysis of their own data as well as that of Bowman et al led Skarsvag (Sk73) to withdraw their initial claims of a 15% scission component. More recent experimental work performed by Blinov et al (Bl73) and Green et al (Gr73) have supported a large, 20-25%, scission neutron component. Green et al also concluded that these scission neutrons are emitted mostly at 90° to the fission axis, while the neutron emission from the fragments is highly anisotropic. The calculations of Madland and Nix (Ma82) mentioned above do not ,however, make provision for an isotropic laboratory neutron component.

1.6. Motivation

Although a large number of measurements of the ^{252}Cf prompt fission neutron spectrum have been made, *"considerable controversy still existis regarding both the shape and the average energy"* thereof (Sp82). The Maxwellian spectrum describes the gross features of the experimental data but systematic deviations are observed. There is also disagreement as to the average energy of such fits to the data. These are found to vary from 2.05 Mev to 2.35 Mev. The most recent measurement (Bo79) yields a value of 2.13 Mev.

Meadows (Me67) concluded that the Maxwellian distribution gave a good representation when only data with energies between 0.5 Mev and 10 Mev were used but that an extension of this curve to lower energies predicted values of N(E) that are of the order of 25% less than the experimental values. In order to study discrepancies between this and other low energy measurements, Jeki et al (Je71) measured the ^{252}Cf neutron energy spectrum over the range 0.002 Mev to 1 Mev. Comparison of their results with those of three other similar measurements can be seen in figure 1.4 . It is apparent that no single Maxwellian temperature is able to fit both the high as well the low energy region.

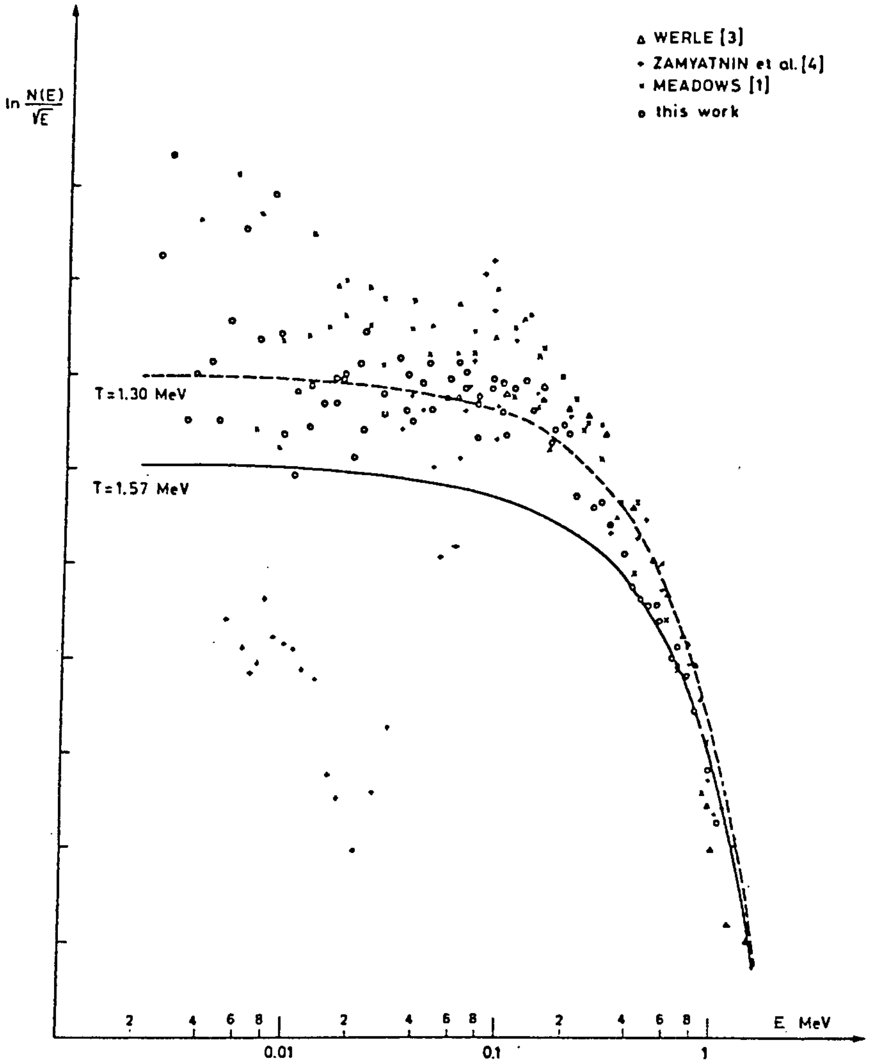

FIGURE 1.4 *Comparison of measurements of the low energy region of the ^{252}Cf fission neutron spectrum. (Figure from Jeki et al, Je71).*

The ^{252}Cf neutron spectrum was measured by Green et al (Gr73) between 0.5 Mev and 13 Mev using long flight paths and pulse-shape-discrimination. Their results indicate systematic variations from a best fit Maxwellian, particularly below 0.7 Mev and above 8 Mev. A three- temperature- per- fragment model (which also attributes 25% of the neutrons to emission from a stationary source) was developed to explain their results. Figure 1.5, taken from their paper, summarises their findings.

Piksajkin et al (Pi78) have reported on the angular distribution of neutrons from ^{252}Cf in the range of angles $0° < \theta < 30°$, where θ is the angle between the neutron trajectory and the fission axis. Their findings are in keeping with the earlier results of Bowman (Bo62), namely, that for ($\theta < 20°$) there are substantial deviations from the hypothesis that 90% of the emitted neutrons are evaporated isotropically from the completely accelerated fragments while the remainder occur at the time of scission. These deviations were attributed by Bowman et al at the time to possible experimental errors resulting from incomplete measurements or to a small number of neutrons collimated along the fission axis.

Piksajkin et al conclude that there is "*an additional mechanism leading to preferential propagation of neutrons along the direction of motion of the fragments*." They suggest that one of the most likely causes of this may be the softening of the neutron spectrum in the restframe of the fission fragment, as neither fragment spin nor "neck retraction" can account for this small angle anomaly. Figure 1.6 shows a calculated fit through their data and that of Bowman et al, modelled on the assumption that there is an excess of low energy neutrons in the fragment restframe system.

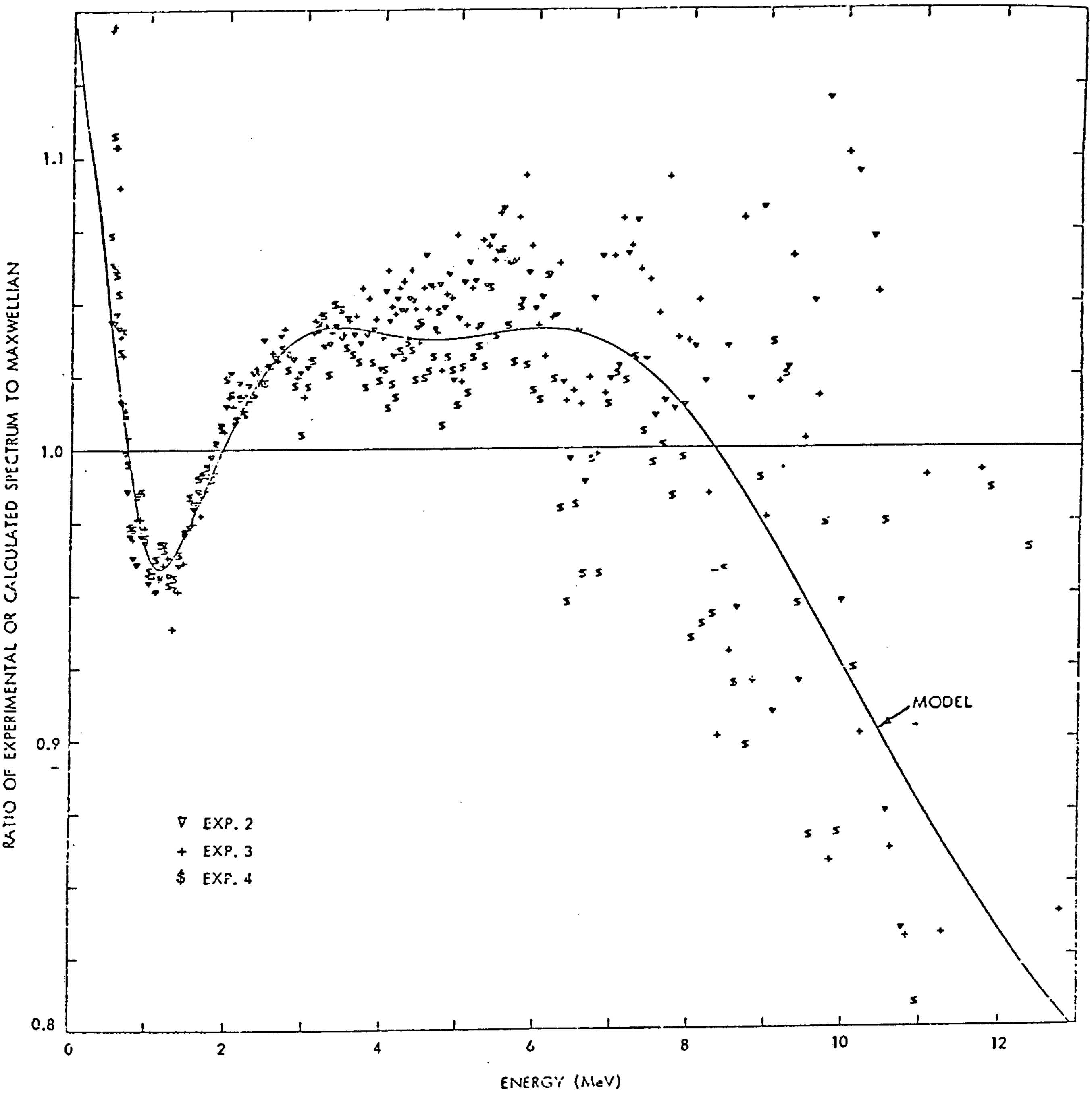

FIGURE 1.5 A measurement of the ^{252}Cf fission neutron spectrum. The points represent ratios of the experimental values to a fitted Maxwellian. The curve shows the prediction of a model developed to fit the data. (Figure from Gr73).

FIGURE 1.6

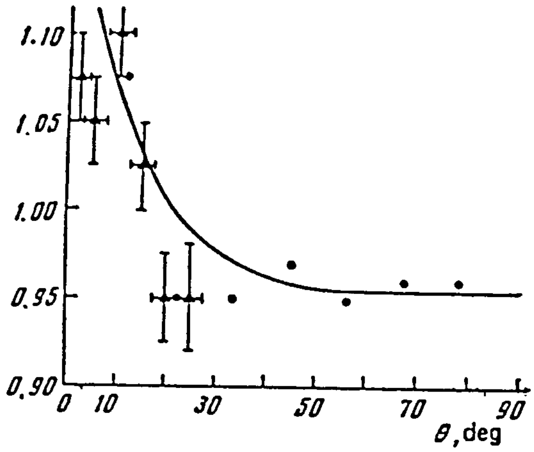

Comparison of measured angular distributions of neutrons from ^{252}Cf with predictions based on the assumption of isotropic evaporation from the fragments. (Figure from Pi78)

● : Ratio of measured values of Bowman et al (Bo62) to the predictions

▲ : Ratio of measured values of Piksajkin et al (Pi78) to the predictions

— : Model developed by Piksajkin et al to explain measurements (See text)

The latest calculations based on standard evaporation theory (Ma82) in which hitherto neglected physical factors are taken into account are still unable to account for all the features of the observed spectra. It is apparent from figure 1.7, taken from the above-mentioned reference that even the calculations allowing for energy dependent cross-sections for compound nucleus formation are not able to follow the low energy trend of the experimental data. (The data are that taken from the recent measurements of N(E) by Boldeman et al (Bo79)). From the preceding discussion it is clear that our knowledge of the prompt neutron spectra in both the laboratory frame and the fragment restframe is still fragmentary. The conflicting data, especially at the low energy ends of these spectra have, as yet, not been resolved. This is largely due to experimental difficulties with regard to low spectral density or background interference. The latter problem is of particular importance in the low energy measurements of the spectrum.

Owing to the extensive catalogue of data on fission that is now available it is possible to exploit the statistical nature of

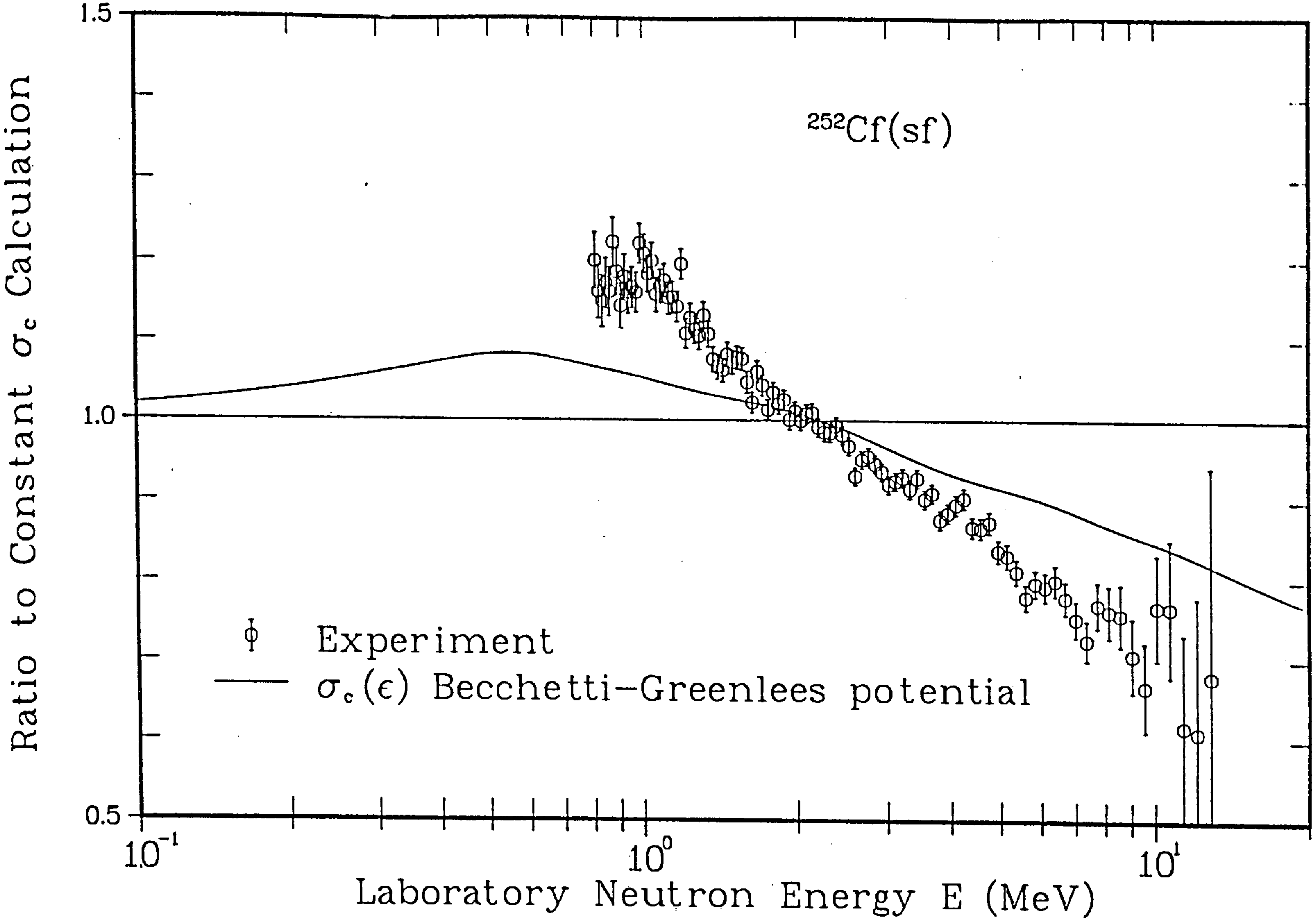

FIGURE 1.7 The ^{252}Cf fission neutron spectrum. The points represent ratios of experimental values to a fitted Maxwellian. The solid curve shows the predictions of Madland and Nix (Ma82). (Figure from Ma82)

neutron emission from fission fragments via Monte Carlo methods. Such calculations have been performed by Pringle and Brooks (Pr75, Pr77) as a convenient means of studying the effects on the neutron spectrum of various forms of anistropic emission and scission neutron components. The outcome of these calculations have, however, pointed to the importance of having as accurate as possible a description of the neutron energy spectrum in the restframe of the fission fragment. Better agreement between simulation and experimental observations were obtained in most cases when a three-component evaporation spectrum was used in place of the simple one-component form. The three-component spectrum was based on the measurements of Bowman et al (Bo62, Bo63) who found that their measurement best fitted an expression of the form:

$$\frac{dN(E)}{dE} = Px\ exp\ (\frac{-x}{p}) + Qx\ exp\ (\frac{-x}{q}) + Rx\ exp\ (\frac{-x}{r}) \qquad (1.5)$$

where $x = E/2T$, E is the neutron energy in the fragment and T is the effective nuclear temperature which is related to the mean neutron energy $\overline{E}$ by the relation $\overline{E} = 2T$. P, Q, R, p, q and r are empirically determined constants. One of the major differences between the three-component spectral form and that of the single -component spectral form is that the former is richer in low energy neutrons than the latter. Figure 1.8 taken from Pringle and Brooks (Pr77) shows the effect on the energy spectrum of the neutrons in the laboratory frame of reference compared with the measurement of Green et al (Gr73). Spectra A and D in the figure were calculated using the three-component form while spectrum P was calculated using the one-component form. In all the cases the calculated spectra are found to be deficient in

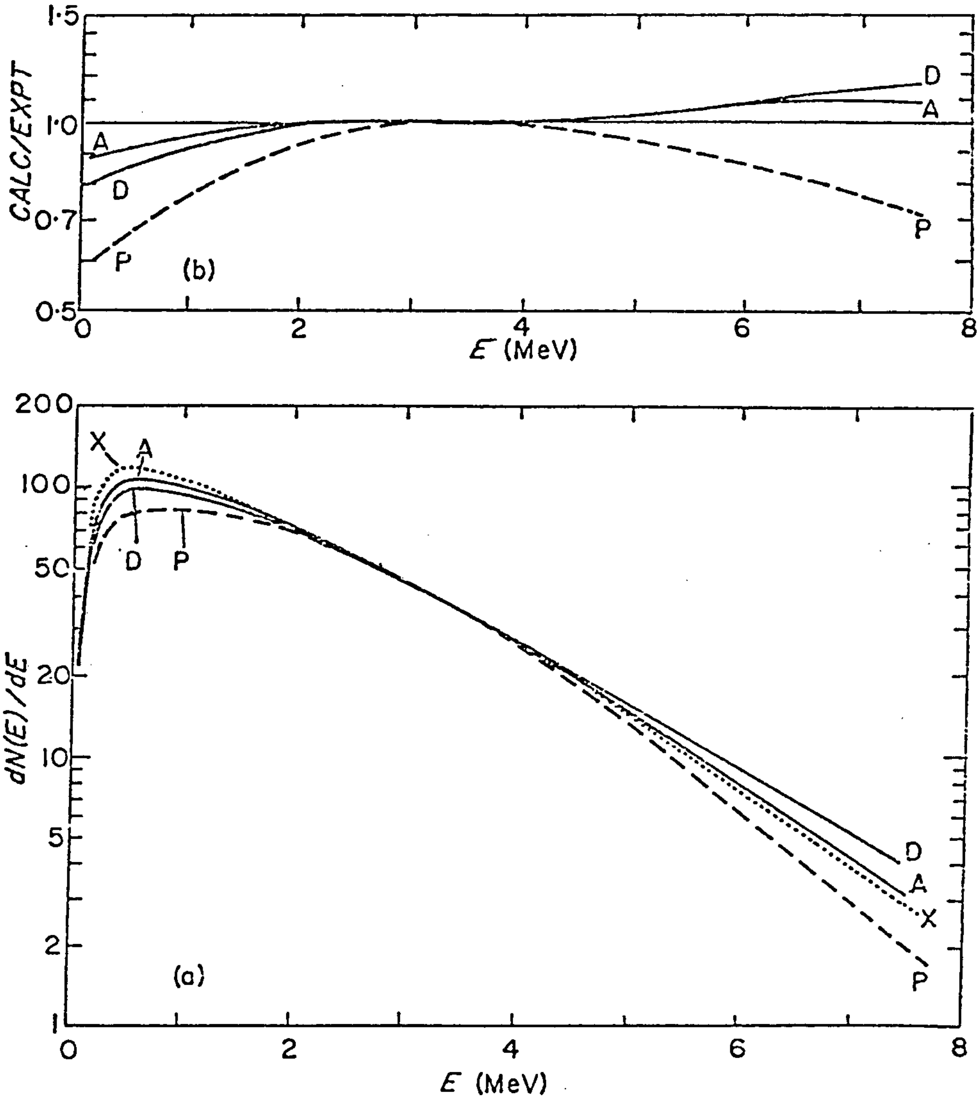

FIGURE 1.8 Laboratory spectrum of neutrons from spontaneous fission of ^{252}Cf showing: (a) empirical fit (curve x) to experimental data (Gr73) and results from Monte Carlo simulations (curves A, D and P) and

(b) ratios of simulated curves A, D and P to the experimental curve X.

(Figure from Pr77)

low energy neutrons compared with the experimental measurement. The agreement is, however, better in the cases of A and D. These observations suggest that the low energy regions of both the energy spectrum in the fragment restframe and the energy spectrum in the laboratory frame be investigated more carefully. We quote from Pringle and Brooks (Pr77):

> *"It is particularly striking that the more prominent discrepancies occur at low neutron energies ... (E_n < 1Mev) and this suggests that the empirical forms used to describe the energy spectrum ... might be inadequate at these energies."*

No measurement, however, of the energy spectrum in the restframe of the fragment appears to have been attempted since that of Bowman et al (Bo62 , Bo63). In view of the preceding discussion as well as in the light of better experimental technology since these measurements were performed it would appear to be an opportune time to undertake a new measurement of the energy spectrum in the restframe of the fission fragment.

To summarise, thus:

The ultimate aims of the programme are to perform accurate measurements of the prompt neutron energy spectrum in the restframe of the fragment as well as in the laboratory frame down to low energies of the order of a few kev. This will allow for a critical comparison to be made between theory and experiment. *The work presented here is an investigation into methods of achieving these aims, in particular, that of measuring the neutron spectrum in the restframe of the fragment.* The methods include the use of the recently developed thin film plastic scintillation detectors in order to measure fragment velocities and the use of a zero-threshold detector for the detection of low energy neutrons.

2. CHAPTER TWO: EXPERIMENTAL METHODS

2.1. Introduction and Notation

In order to calculate the prompt neutron energy spectrum in the restframe of the parent fission fragment, it is necessary to establish the velocity of the neutron in the laboratory frame of reference as well as the velocity of the associated fragment. A vector subtraction of these quantities will determine the velocity of the neutron in the restframe of the fragment. Hence the energy of the neutron in the restframe of the fragment can be determined.

For clarity we will designate two hemispheres or directions called FORWARD and BACKWARD defined by the positions of the neutron detector and the ^{252}Cf source, as shown in figure 2.1. Thus, in any fission event one fragment will be emitted into each of these hemispheres. We will, thus, refer to *forward fragments* and *backward fragments* in the discussion. In the special case where the angle between the centre of the fragment detector and the centre of the neutron detector is 90 degrees the fragments will be emitted equally into both hemispheres. We will refer to this as the BROADSIDE orientation. The notation that will be used throughout this work is summarised in table 2.1.

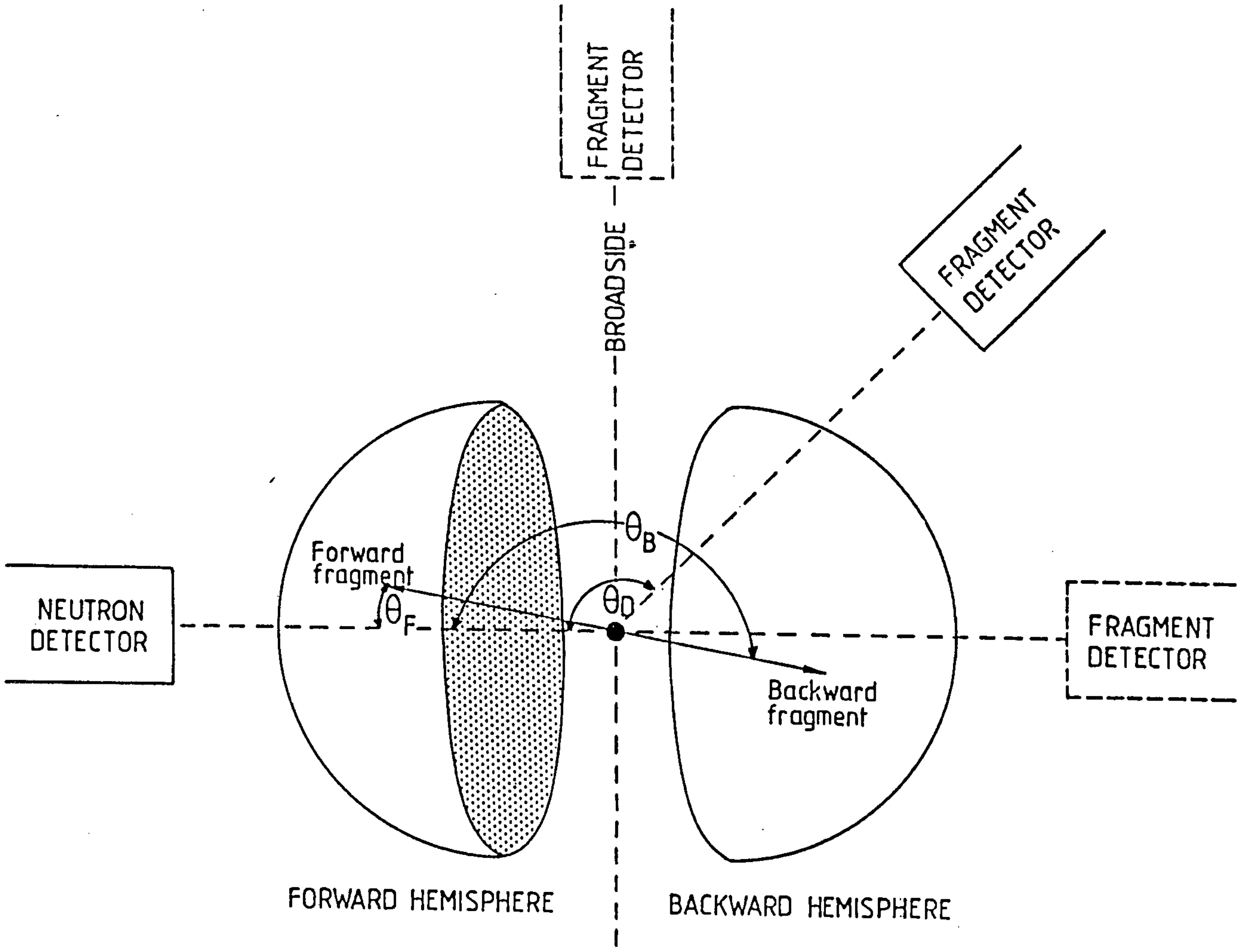

FIGURE 2.1 Diagram showing the FORWARD and BACKWARD hemispheres as defined by the position of the neutron detector. Each fission event gives rise to a forward fragment and a backward fragment except in the case where the fragment detector is placed in the BROADSIDE position.

TABLE 2.1

V_F : the velocity of the forward fragment in the laboratory frame

V_B : the velocity of the backward fragment in the laboratory frame

v : the velocity of the neutron in the laboratory frame

v_{PF} : the velocity of the neutron in the restframe of the forward fragment

v_{PB} : the velocity of the neutron in the restframe of the backward fragment

Θ_F : the relative angle defined by the directions of V_F and v

Θ_B : the relative angle defined by the directions of V_B and v

Θ_P : the relative angle defined by the directions of V_F and v_{PF} or by the directions of V_B and v_{PB}

Θ_D : the angle between the neutron and the fragment detectors

E : the energy of a neutron in the laboratory frame

E_{PF} : the energy of a neutron in the restframe of the forward fragment

E_{PB} : the energy of a neutron in the restframe of the backward fragment

Summary of the notation used in this work.

2.2. The design of the experiment

A standard technique for determining the velocities of neutrons is the time-of-flight method in which the flight of a neutron is timed over a known distance, the flight path. This requires a detector which is placed at the end of the flight path as well as detector to provide a time-zero signal. The same technique can also be used to measure the velocities of the fission fragments. However, with the advent of the thin film plastic scintillation (TFPS) detector a more convenient way of obtaining information on the fragment velocity is now available. The velocities of the fragments are simply determined from the scintillation response of the TFPS detector to the fragments.

The TFPS detector also serves, conveniently, as a time-zero detctor for the neutron measurement. Since a negligible fraction of the fragments travel slower than 0,7cm/ns (Wh63) the TFPS detector is adequate as a time-zero detector providing that it is placed close enough to the fission source. A maximum timing error of less than 1ns will result if the distance between the TFPS detector and the source is about 0,5cm. A more detailed discussion on TPFS detectors as well as on the choice of the neutron detector is provided in chapter 3.

Now, each detected neutron of velocity, v, could have been emitted by either the forward fragment or the backward fragment associated with the fission event. The transformation of v to a velocity in the restframe of the fission fragment can, therefore, lead to either v_{PF} or v_{PB} depending on which one of the two fragments is assumed to have been the parent fragment of the detected neutron. By choosing the geometry carefully, it is possible to reduce the uncertainty in this assignment to a considerable degree. Even though the neutrons may be evaporated isotropically from each fragment (Bo62) the translational kinetic energy of the fragment results in the neutron distribution in the laboratory frame being forward peaked in the direction of motion of the fragment, as shown in figure 2.3. This behaviour is also reflected in the measurements of the angular distribution of the neutrons in the laboratory frame as shown in figure 2.2.

Thus, if a neutron and a coincident fragment are detected at 0° relative to each other, it is highly likely that the neutron was emitted by the forward fragment. Feather and Vass (Fe75) have calculated that for a small solid angle centred around $\Theta_D = 0°$ (i.e. the detected neutron is travelling parallel to the forward fragment) the assignment of the forward fragment as the parent is incorrect, *on average*, once in every 500 times. A similar ratio, 0,3%,was estimated to be the case by Bowman et al (Bo63) during their measurements which were performed at $\Theta_D = 11.25°$.

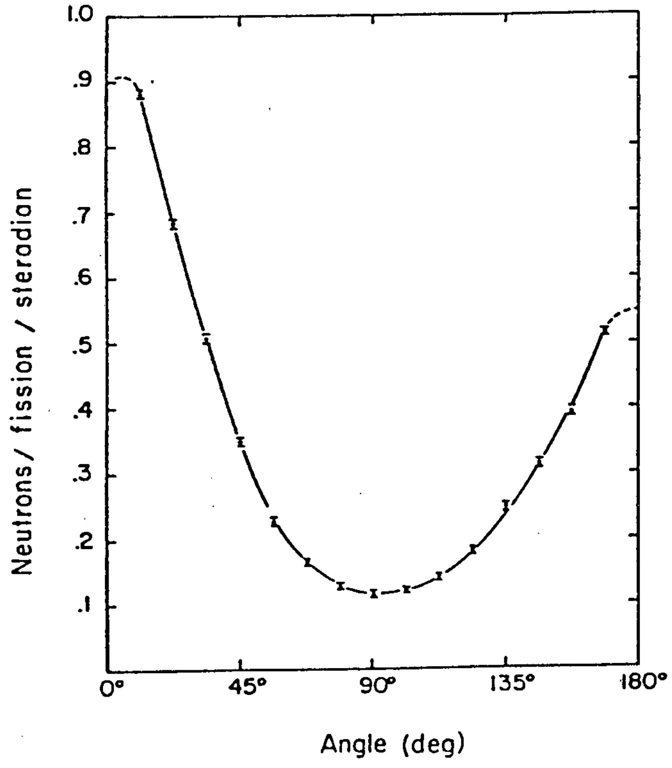

FIGURE 2.2

The measured angular distribution (laboratory frame) of neutrons from ^{252}Cf (sf) relative to the fission axis, with the light fragment along 0° and the heavy fragment along 180° (Figure from Bo62)

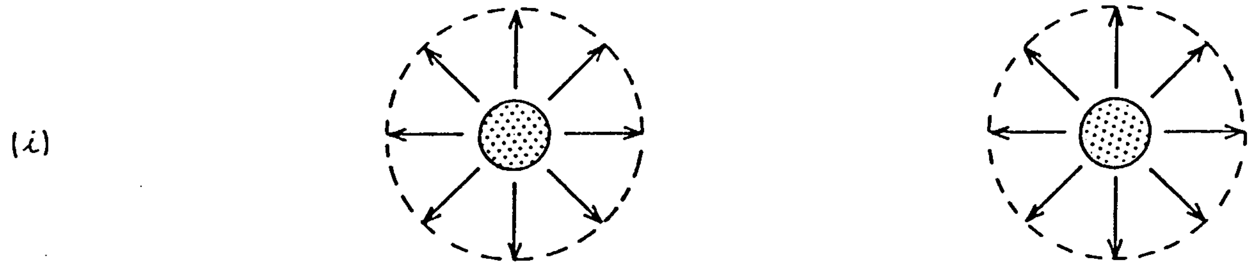

The arrows represent the velocities of neutrons emitted isotropically in the restframes of their parent fragments, assuming an average neutron velocity of 1.7 cm/nsec (Bo62) in this frame.

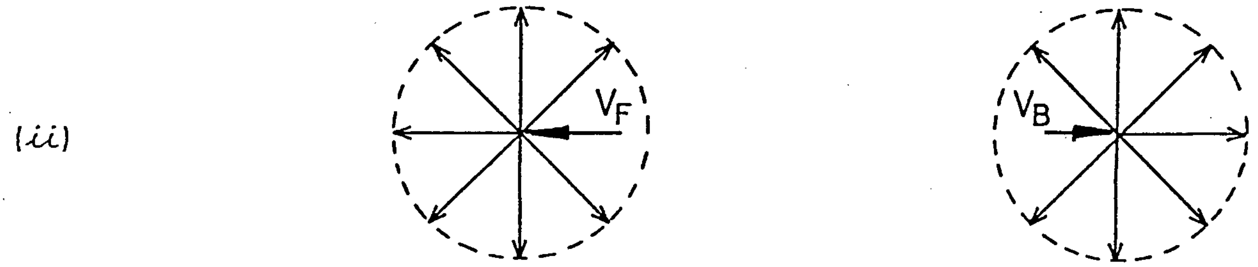

In the laboratory frame the velocity of the neutron is the vector sum of its velocity in the fragment restframe and the velocity of the parent fragment.

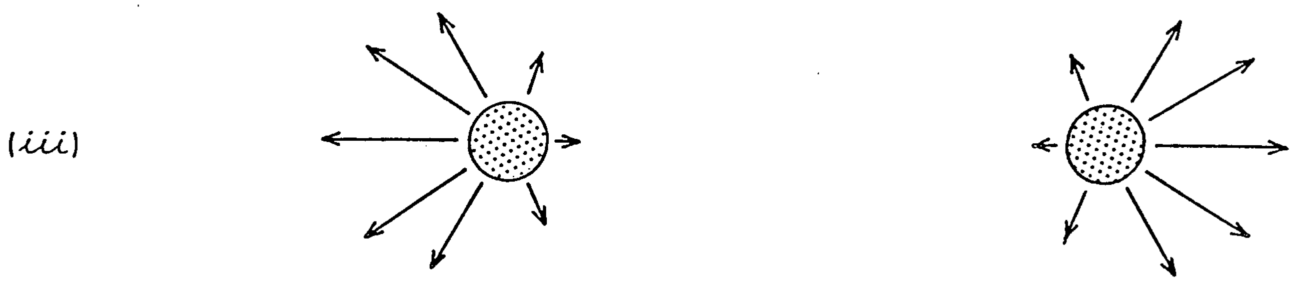

The arrows represent the velocities of the neutrons in the laboratory frame. The neutron distribution is forward peaked in the direction of motion of the parent fragment.

FIGURE 2-3 Schematic diagram illustrating the effect of fragment motion on the neutron angular distribution in the laboratory frame.

In our experiment, since the TFPS detector was being used both as a fragment detector and as a time-zero detector for the neutrons, it was not convenient to set $\Theta_D = 0°$. Setting $\Theta_D = 0°$ would have required that the detected neutrons pass through the photomultiplier tube of the fragment detection system. Instead, Θ_D was set at 180°, so that the backward fragments were detected. Based on the assumption of the collinearity of the pair of fragments in a binary fission event, the neutrons that are detected can be regarded as having being emitted from the forward fragment, i.e. $\Theta_F = 0°$, to within the limits just mentioned.

Clearly the chance of correctly assigning the fragment to the neutron decreases as the neutron detector is moved towards the broadside orientation. However, in the special case of symmetric fission, $V_F \simeq V_B$, and hence $V_{PF} \simeq V_{PB}$ so that the ambiguity in the assignment of the parent is irrelevant. Militating against this is the fact that symmetric fission is rare and extremely long running times would be required to obtain good statistical accuracy.

In order to obtain the neutron spectrum in the laboratory frame of reference a measurement was required at some intermediate angle. Data were thus collected at a Θ_D angle of 130°, i.e. $\Theta_B = 130°$ and $\Theta_F = 50°$.

2.3. Outline of the method

Figure 2.4 shows, schematically, the geometrical configuration that was used for the experiment. The neutron spectrum from the spontaneous fission of ^{252}Cf was measured at the three angles Θ_D = 180°, 130° and 90°. This was achieved by rotating the neutron detector to the required angle, Θ_D, as indicated. The neutrons were detected in coincidence with their associated fission

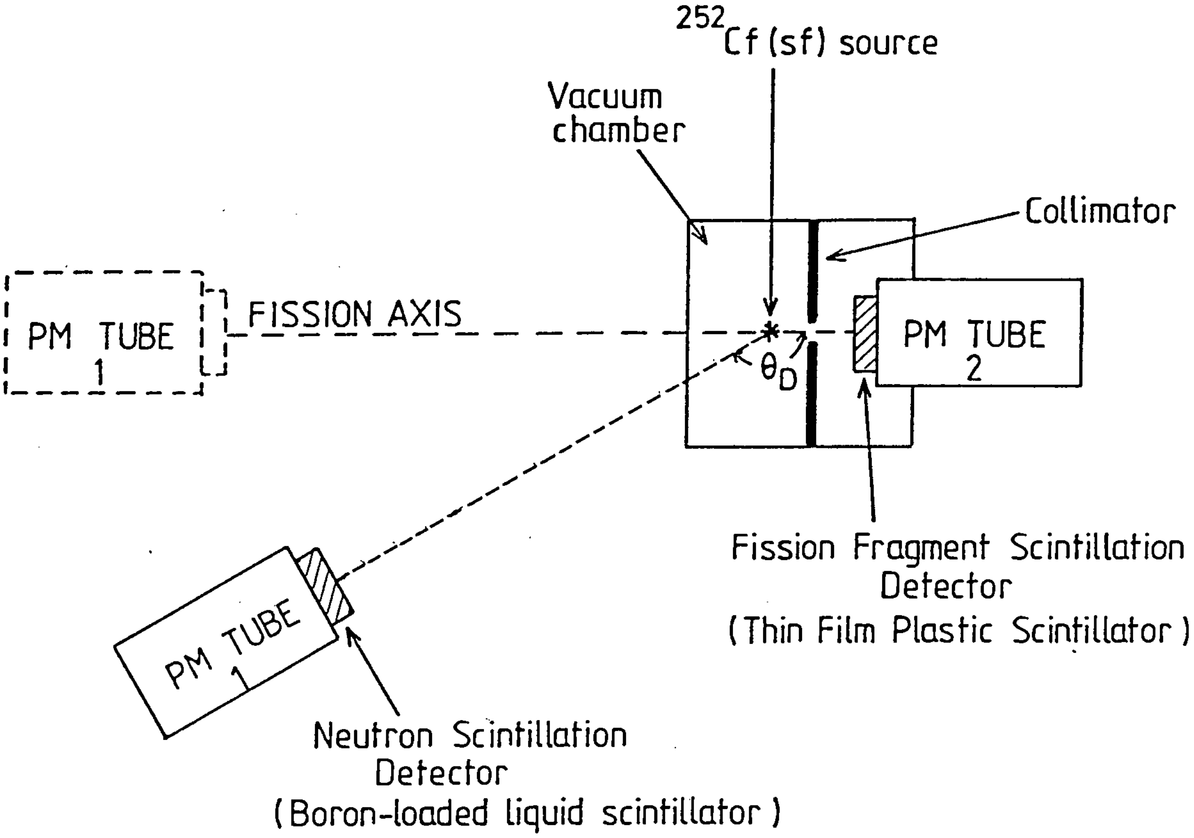

FIGURE 2.4 *Schematic diagram of the experimental geometry. Neutrons are detected in coincidence with associated fragments. Fragment velocity is determined from a TFPS detector while neutron velocity is measured by time-of-flight.*

fragments at the end of a 20cm flight path. In order to select the direction of the fission fragments a collimator was placed in front of the source. The following parameters were recorded event-by-event on magnetic tape :

(i) neutron time-of-flight (T pulse)

(ii) neutron detector pulse height (L pulse)

(iii) fragment detector pulse height (F pulse)

These multiparameter measurements were performed at the Southern Universities Institute (SUNI). The data were collected on SUNI's SUREAL data acquisition system over a continuous period of four weeks. More than half of the time was spent at the configuration in which $\Theta_D=180°$. The average data rates that were involved were between 5 and 6 events per minute. The data were subsequently analysed off-line on UCT's UNIVAC computer.

2.4. The sources

The californium-252 source that was used was an electrodeposited layer of californium on gold backing. This source allows fission fragments to be emitted normally with no energy loss on the "open" side of the source. Thus, in the case of binary fission one fragment will escape while its co-fragment will be absorbed in the source backing.

A summary of the major characteristics of californium-252 is given below (from (Ia74)).

Atomic number 98

Atomic weight 252

Half-life for alpha emission 2.73 years

Half-life for spontaneous fission 85.5 years

Half-life 2.65 years

Fraction of decays by alpha emission 97%

Fraction of decays by spontaneous fission 3%

Average number of neutrons per spontaneous fission 3.8

Decay heat (51% from fission, 49% from alpha decay) 39 μW/μg

Specific activity 530μCi/μg

Thus, the 1 μCi source used produced about 1000 fissions per second spread into a solid angle of 4π steradians.

For the purposes of calibration and the setting up of the pulse-shape-discrimination circuitry an americium-241/ beryllium (^{241}Am/Be(α,n))source was used to provide a large neutron flux. The 200 mCi that was employed provided 5×10^5 neutrons per second into 4 π steradians and consisted of a mixture of americium oxide with beryllium metal doubly encapsulated in welded stainless steel. A wax shield surrounding the Am-Be source acted as a moderator.

2.5. The fragment detector

The fragment detector was an organic scintillator, in the form of a thin plastic film. Preliminary experiments were performed using semiconductor detectors as well as NE102 plastic scintillator. In the case of the semiconductor detectors radiation damage severely limits the running times, while the ordinary plastic scintillator is unable to resolve the alpha particles, the heavy fission fragments and the light fission fragments into easily distinguishable components in a pulse height spectrum. The use of thin film plastic scintillation, TFPS, detectors offers a solution to these problems. We discuss these detectors in more detail in chapter 3.

2.6. The Neutron Detector

The neutron detector, NE321, was a liquid organic scintillator loaded with boron. The detection liquid was encapsulated in a cylindrical glass cell one and a half inches in diameter and one inch thick with an expansion chamber rising from the side wall. The scintillator was mounted on a photomultiplier tube 5cm in diameter. Optical coupling was effected by the use of silicon oil. The photomultiplier was surrounded by a cylindrical mu-metal covering to shield it from the earth's magnetic field.

Since the scintillator consists mostly of hydrogen and carbon atoms, high energy neutrons can undergo elastic scattering with the hydrogen nuclei. During this process the neutron transfers part of its kinetic energy to the proton giving rise to a recoil proton which in turn can give rise to the fluorescence required for scintillation detection. The maximum energy which can be transferred from slow neutrons, however, is small so that the resulting recoil nuclei are too low in energy to generate a usable detector signal. In order, thus, to be able to detect neutrons down to low energy it is necessary to supplement the recoil detection by an additional detection mechanism. One way of achieving this is by using a boron-loaded liquid scintillator. Detection of slow neutrons is now able to proceed via the $^{10}B(n,\alpha)$ capture reaction, the details of which are as follows (Ja65):

Reaction	Q-value (Mev)	branching ratio (%)
$^{10}_{5}B + ^{1}_{0}n \longrightarrow ^{7}_{3}Li + ^{4}_{2}\alpha$ (ground state)	2.8	7
$^{7}_{3}Li^{*} + ^{4}_{2}\alpha$ (excited state)	2.3	93
$\downarrow$		
$^{7}_{3}Li + \gamma$ (477.6 keV)		

The energy of the α-particle which is emitted has a value of about 1.5 MeV in the case of the second reaction, while the α-particle associated with the ground state lithium is higher by about 20%. The resulting light pulse which is produced by these ionising particles is equivalent to that produced by an electron with an energy of about 40kev (Bo57). The utility of this reaction stems from its large, structureless cross-section, which, essentially, is inversely proportional to the velocity of the neutron. The cross-section has a value of 3840 barns for thermal neutrons (Ko79). By combining the two detection mechanisms described, the resulting zero-threshold neutron detector is useful for measuring neutrons over a a wide range of energies.

2.7. Electronic Configurations and Data Collection

A schematic diagram showing the major components of the electronic configuration that was used for data collection is shown in figure 2.5.

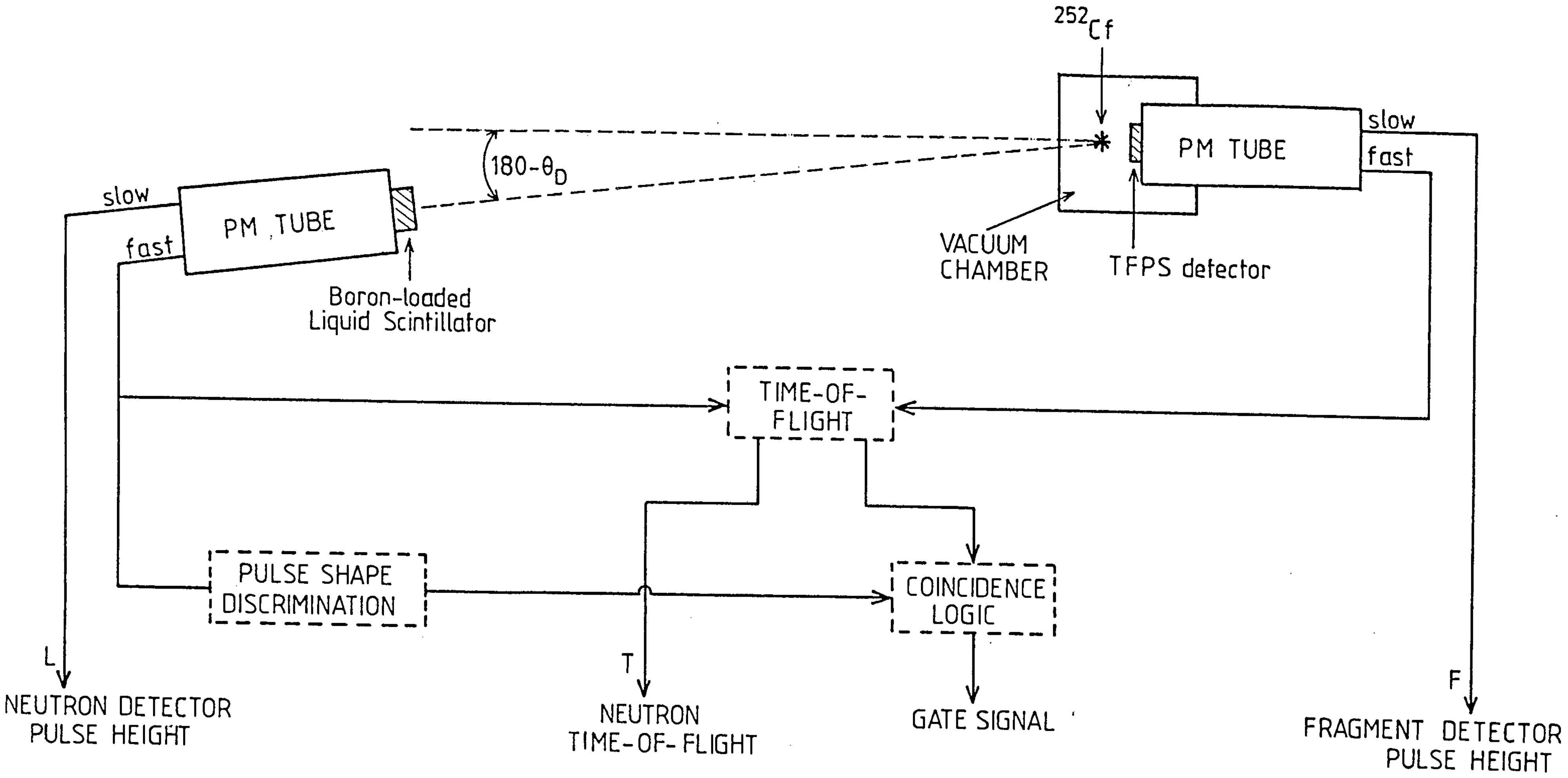

FIGURE 2.5 *Schematic diagram of electronic configuration. Gamma rays detected by the liquid scintillater are rejected by Pulse Shape Discrimination. A three-parameter event is recorded on buffer tape when a gate signal is produced by the Coincidence Logic.*

The neutron detector provides two output signals : (i) L, the linear pulse arising from either the energy of the recoil proton or from the sum of the proton and α particle energies in the case of the B(n,α) reaction (ii) a fast timing output. The fragment detector provides (i) a linear, pulse F, which is derived from the light output of the thin film plastic scintillation detector and (ii) a fast timing output.

The major features of the configuration are:

(i) linear pulse processing for each of the L and F pulses,
(ii) pulse shape discrimination to distinguish between gamma rays and neutrons,
(iii) the neutron time-of-flight measurement and
(iv) coincidence gating

The block diagram, figure 2.6, shows in detail the electronic circuitry used to process these signals.

2.7.1. Pulse Shape Discrimination

In order to distinguish between gamma rays and neutrons so that the number of events associated with gamma rays can be reduced the neutron detector was equipped with pulse shape discrimination, PSD, circuitry (Br59). A "Link PSD 5010" system provided the necessary circuitry in one electronic NIM compatible module (Ad78). The PSD method employed is that of comparison between the amount of light in the tail of the pulse and that in the entire pulse.

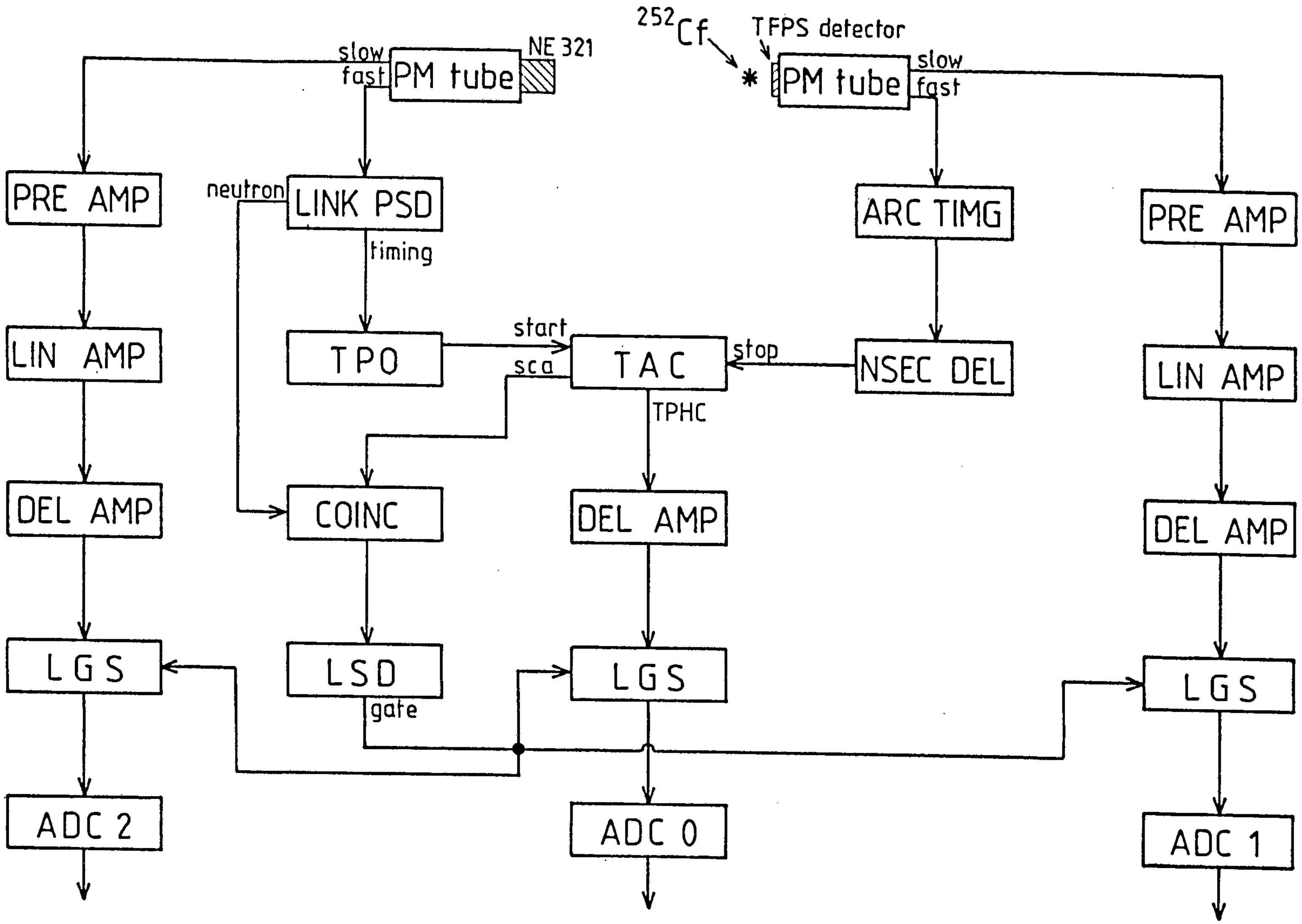

FIGURE 2.6 *Block diagram of the electronics. The outputs from the ADC's were routed to a PDP 11/34 computer and stored on magnetic tape.*

2.7.2. Time-of-flight Measurements

A TFPS detector mounted on an RC8575 photomultiplier tube registered the passage of the fission fragments. The "fast" timing pulse arising from this detector is adequate as a time-zero signal for the time-of-flight measurements, since the ^{252}Cf source was situated less than a centimetre from the TFPS detector. The signal, however, was delayed to provide the "stop" signal to the time-to-amplitude converter,TAC, while the neutron detected at the end of the flight path was used as the "start" input. The reason for using this method of operation is to reduce the number of false "starts", since the number of fragments detected exceeds the number of neutrons detected by about two orders of magnitude. The time axes of resultant distributions are thus reversed with respect to the "pulse height" registered by the TAC as demonstrated in figure 2.7 .

2.7.3. Data Collection

The raw data consisting of the three parameters T, L and F per event were dumped automatically to magnetic tape via the SUREAL data acquisition system at SUNI. Each parameter was digitised to a number between 1 and 4096. At the same time the data were monitored in the form of one and two parameter spectra. These spectra were written to a separate magnetic tape at suitable intervals.

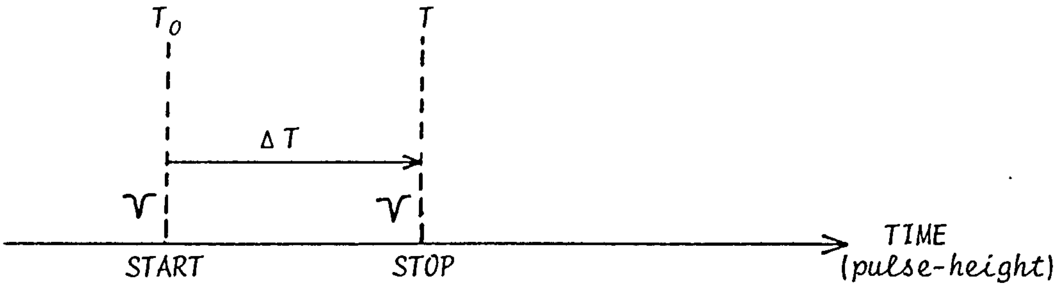

(i) Pulse-height is proportional to ΔT

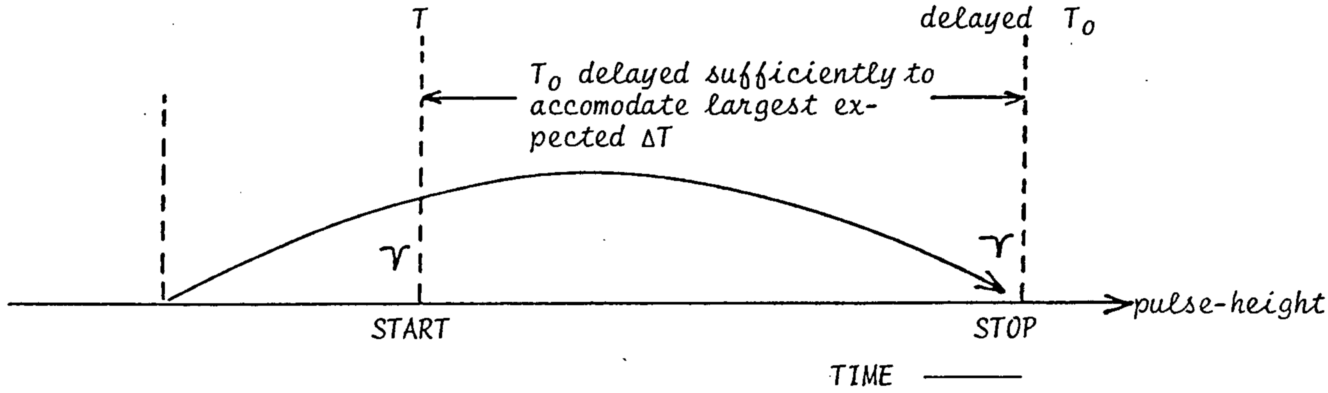

(ii) The trigger from the time-zero detector, T_0, is delayed to act as the STOP pulse.

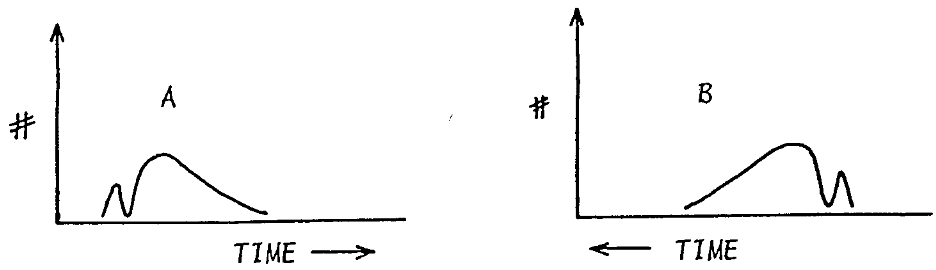

FIGURE 2.7 The true time-of-flight axis is reversed with respect to the pulse-height axis. Thus the "true" time spectrum, A, appears as shown in B.

2.7.4. Calibrations

Various calibrational checks were carried out before the start of each run set as well as at the end of the run.

(i) Time-scale calibrations were performed by introducing calibrated nanosecond delays into the "stop" pulse input of the TAC. With the gamma discrimination turned off the position of the gamma peak was noted with and without the delay.. The latter peak position also allowed time-zero to be determined as the flight time over the time-of-flight distance is easily calculated. A second method was used in which the fragment time pulse was used for both the "start" and the "stop" inputs for the TAC. The shift of the "spike" in the T-spectrum due to the delays allowed the time axis to be calibrated.

(ii) The position of the boron peak in the neutron pulse height spectrum, L parameter, due to the B(n,α) reaction was checked by using an Am-Be source (section 2.4) surrounded by a wax moderator. True-zero was found in the L-pulse spectrum by noting the position of the peak for different settings of the amplifier gain.

(iii) A "singles" fragment pulse height spectrum was also recorded.

(iv) Short runs were recorded at longer and shorter flight paths than for the "actual" runs in order to check for time-walk effects.

In the following chapter we discuss the calibration of the TFPS detector and the measurement of the efficiency of the neutron detector for incident neutrons of low energies.

3. CHAPTER THREE: CALIBRATION OF THE DETECTORS

3.1. The Neutron Detector Efficiency

In order to measure the energy spectrum of the neutrons in either the laboratory frame or in the fragment restframe we require a knowledge of the efficiency of the neutron detector. In the case of proton recoil detection it is relatively easy to calculate the absolute efficiency, $\varepsilon(E)$, as a function of energy using, for example, the equation (Ow60):

$$\varepsilon(E) = \frac{E-E_B}{E} (1 - exp(-n_H \sigma_S(E)d)) \qquad (3.1)$$

where E = energy of the incident neutron

E_B = neutron detection threshold

n_H = number density of protons in the scintillator

$\sigma_s(E)$ = n-p scattering cross-section at energy E

d = mean scintillator thickness

Two effects that are neglected in this equation are: (i) the scattering off carbon nuclei and (ii) the possibility of multiple n-p scattering. For our scintillator the following values were used in the calculation:

$n_H = 47.5 \times 10^{21}$ H atoms/cm^3, $d = 2.54$ cm, $E_B = 0.250$ MeV

An emperical fit to the n-p scattering cross-section was used viz., (Ma68 quoted in Kn79)

$$\sigma_S(E) = \frac{4.83}{\sqrt{E}} - 0.578 \qquad (3.2)$$

where σ_S is measured in barns and E in MeV (Ma68 cited in Ko79). Since our detector, however, is able to detect neutrons down to zero energy on account of the capture reaction which dominates at the lower neutron incident energies it is not possible to calculate the efficiency in these regions as easily as for the case of the proton recoil detection. In order to extend the efficiency curve down to these regions the efficiency relative to that of 12.7 mm thick lithium-loaded glass scintillator was measured. A schematic diagram of the experimental arrangement used for the measurements is shown in figure 3.1.

The neutron source was the ^{7}Li (p, n) ^{7}Be reaction produced by protons from the pulsed Van de Graaff accelerator of the Southern Universities Nuclear Institute. By varying the incident proton energy on the thin lithium metal target used, various well-defined neutron energies were obtained. The two scintillators mounted on photomultiplier tubes were placed symmetrically at an angle of 10° from the proton beam direction, so as to receive the same mean incident neutron energy and flux from the (p,n) source. A thin (∿2mm) lead sheet was placed between the target and the scintillators in order to shield the scintillators from the large low-energy gamma ray flux originating from the target.

A block diagram showing the components of the electronic circuitry that was used is shown in figure 3.2. Two "fast" signal processing chains, one from each detector, were used to obtain

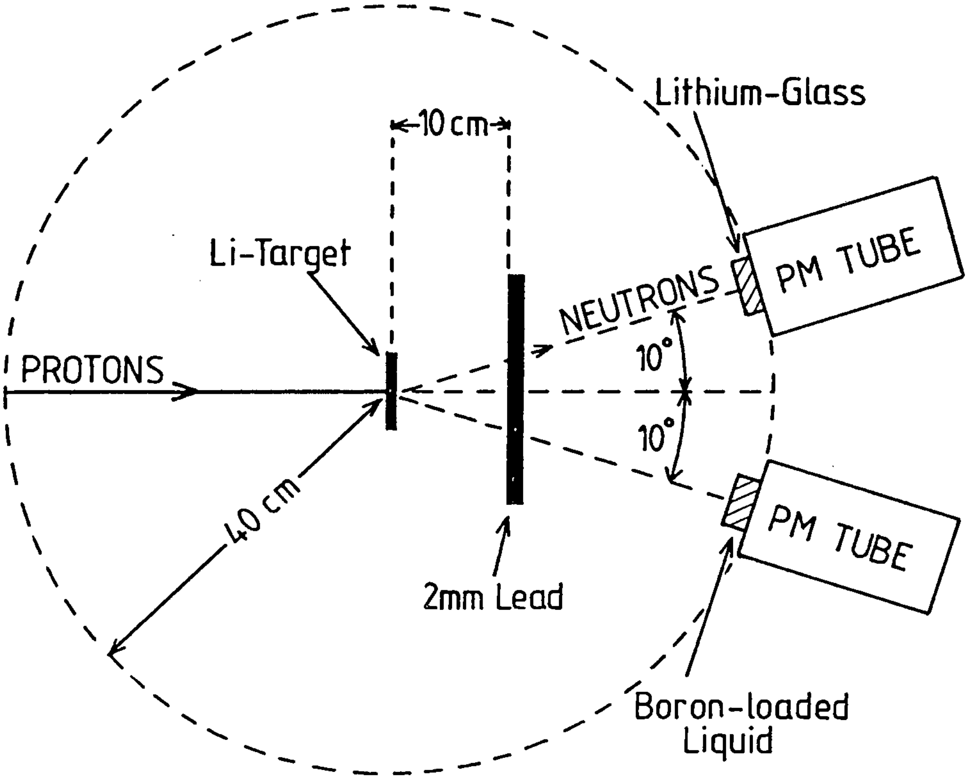

FIGURE 3.1 *Schematic diagram of the experimental arrangement used to measure the efficiency of the boron-loaded liquid scintillator relative to that of a lithium/loaded glass scintillator.*

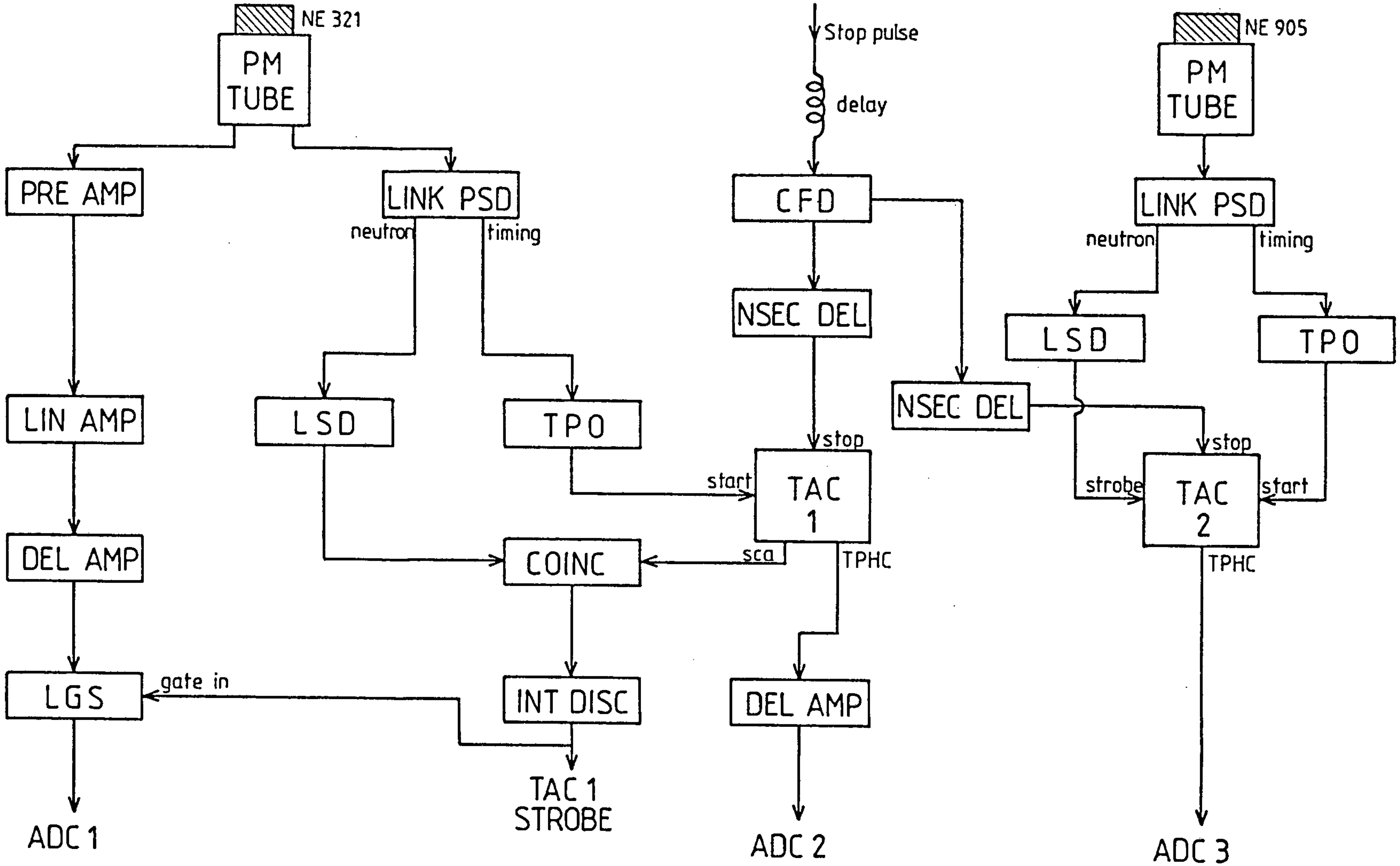

FIGURE 3.2 *Block diagram of the electronics used for measuring the efficiency of the boron-loaded liquid scintillater relative to that of a lithium-loaded glass scintillater.*

time-of-flight spectra from the two detectors. In both cases the "stop" inputs for the time-to-amplitude converters, TACs, were provided from a suitably delayed signal originating from an electronic pickup sensing the proton "bunch" at the end of the beam line. In the case of the boron loaded scintillator, a Link PSD 5010 unit provided the required pulse-shape-discrimination, PSD, circuitry. (See section 2.7.1). The "neutron" output from the PSD unit together with the SCA output from the TAC were used in coincidence to provide a "strobe" pulse to the TAC as well as to provide a gate for the linear L-pulse from the "slow" output of the boron-loaded detector. The PSD unit used to process the signals from the boron-loaded liquid was tuned to the settings that were used in the previous experiment, (chapter 2). The PSD unit used on the lithium-loaded glass side of the electronics was used largely to symmetrise the electronics of the two detection systems.

Checks on the pulse-height windows of both detectors were performed at regular intervals between the various runs. In the case of the boron-loaded liquid this included using the Am-Be neutron source placed in wax (section 2.4) as well as using an Americium-241 source which emits a 60kev gamma ray. The checks on the lithium-loaded glass were performed with the Am-Be source and the 1.17MeV gamma ray emitted from a Co-60 source.

For a run at a particular neutron energy two time-of-flight spectra are obtained, one for each detector. The areas under these curves, A_{Boron} and $A_{Lithium}$, can thus be determined. These areas are, of course, proportional to the counts rates of their respective detectors. Several such pairs of spectra were obtained for a series of neutron energies ranging from 35 KeV to 500 KeV.

At each energy the count rate ratio, R, was calculated. The relative efficiency, $E_B(E)$, for the boron-loaded liquid at neutron energy E was thus calculated from the expression:

$$\varepsilon_B(E) = R\varepsilon_{Li}(E)$$

where $R = \dfrac{A_{boron}}{A_{lithium}}$

and $\varepsilon_{Li}(E)$ *is the calculated efficiency of the lithium-glass scintillator.*

The efficiency of the boron-loaded liquid scintillator over the energy range 35 keV to 10 MeV is shown in figure 3.3. The curve comprises the measurements as well as the calculations according to equation 3.1.

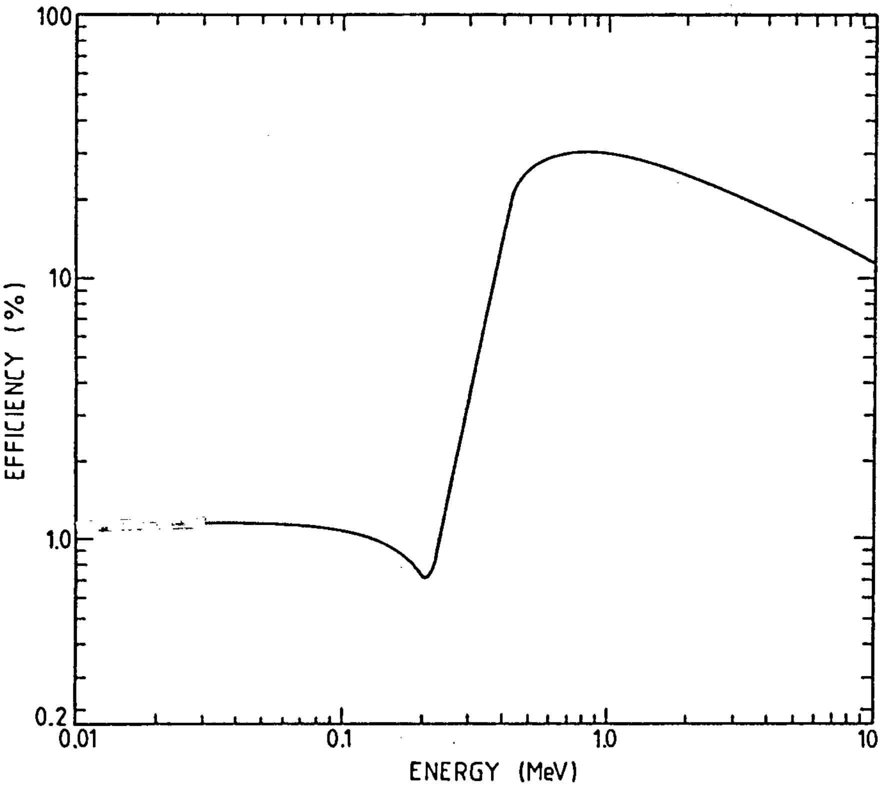

FIGURE 3.3 *The efficiency of NE321 boron-loaded liquid scintillator as a function incident neutron energy. Both axes are plotted on logarithmic scales.*

3.2. Thin film plastic scintillation detectors

3.2.1. Introduction

Thin film plastic scintillation, TFPS, detectors were first described in use as time-of-flight particle detectors to register the passage of very heavy ions such as fission fragments (Mu70). A TFPS detector is ordinary plastic scintillator such as NE102 which has been reduced to a thickness ranging from about 10μg/cm^2 to several tens of thousands of μgs/cm^2. Various techniques for making these films have been described all of which involve the use of organic solvents (Mu72), (Go74), (Ba75), (Aj76), (Ge77).

Radiation such as a fission fragments impinging on a TFPS detector excites rotational, vibrational and electronic states of molecules by (a) direct Coulombic interaction and (b) indirectly by the "spray" of recoil electrons generated by the fragment (Mu70, MU74). The amount of energy lost by a transiting fission fragment in a scintillator foil will of course depend on the thickness of the foil. For example ^{252}Cf (sf) fission fragments passing through a 400μg/cm^2 thick film are degraded by about (11-15)% (Mu72) which represents an energy loss of between 10 and 15 MeV, while a 10μg/cm^2 thick film has an effect which is an order of magnitude smaller.

3.2.2. Time resolution and pulse height response.

Muga (Mu70) reported that the time spread inherent in a TFPS detector fabricated out of NE102 plastic was 0.90 nsec (FWHM). Various studies with light ions (Mu73a, Ko75, Ke 78), heavy ions

(Mu73c, Mu75) and fission fragments (Mu70, Mu73b, Mc74) have indicated that the TFPS pulse height response depends almost solely on:

(1) the nuclear charge, Z and

(2) the velocity of the impinging radiation.

Furthermore, in the case of fission fragments, the pulse height response is reported to be proportional to the velocity of the transiting particles (Mc74). The degree of separation between the alpha particles, the heavy (slow) fragment group and the light (fast) fragment group depends on the thickness of the detector. We show this effect in figure 3.4 taken from reference Aj76.

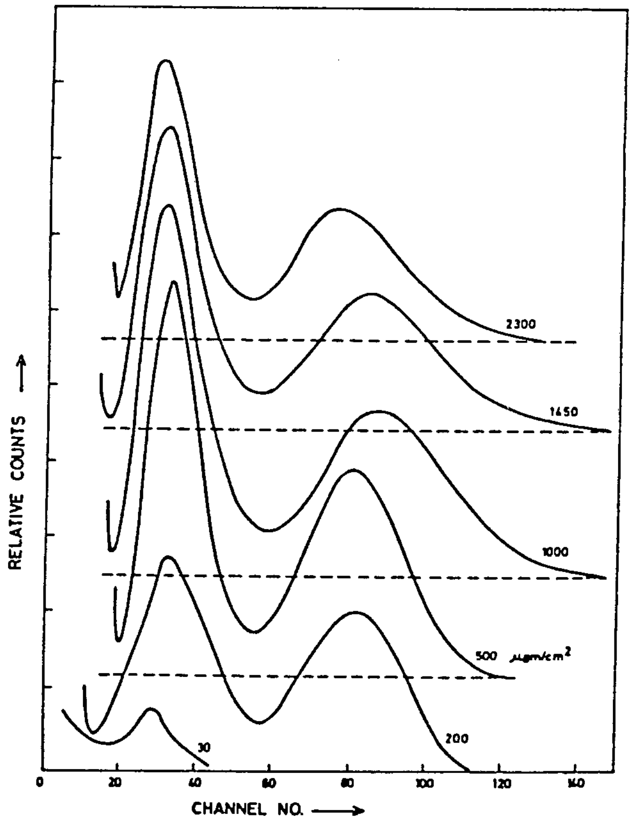

FIGURE 3.4

Pulse-height distributions obtained from TFPS detectors of different thicknesses when irradiated with fission fragments from ^{252}Cf (sf).

(Figure from Aj76)

3.2.3. Summary of useful features for detecting fission fragments.

(1) 100% efficiency in most cases. This is an important feature in experiments such as the one reported in this work where the event rate is low.

(2) Good signal-to-noise ratio.

(3) Simplicity and low cost of fabrication. (See section 3.2.4).

(4) High counting rate capability.

(5) Insensitivity to gamma radiation.

(6) Absence of radiation damage problems. This feature makes the detector attractive for our work, since the more conventional semiconductor detectors used for fragment detection are unable to withstand very long exposures to heavy ions.

(7) Fast time response.

(8) Small energy loss.

(9) The scintillation pulse height response is velocity dependent. This is one of the most important features of the detector relevant to this work.

Although the usefulness of TFPS detectors in fission investigations has been pointed out about ten years ago, very little work has been reported in which these detectors have been utilised. This is probably largely due to the fact that all the features of TFPS detectors are not yet fully understood. There is also not complete agreement on those characteristics that have been reported, especially where different methods of fabrication have been employed or where different light collection geometries have been used. For the purposes of this work, in which we need to determine the velocities of fission fragments, it was thus found necessary to perfom experiments in which the TFPS detector response was studied as a function of fragment velocity. In the sections below, we describe our experiments with TFPS detectors and their response to fission fragments.

3.2.4. Fabrication of TFPS detectors.

Our first TFPS detectors were made using the recipe of Muga et al (Mu72) according to which a few grams of NE102 are dissolved over a period of a few hours in a mixture of ethyl acetate and amyl acetate. A few drops of this solution are then spread onto a surface of water leaving a thin layer of plastic floating on the surface. In order to obtain films of uniform thickness the method of stretching the water surface by placing an "O-ring" on the surface (Ba75) was used. Although a few films were produced via this method the rate of success was not very high. Problems were encountered with the solution itself which would often not spread at all on the water surface. This occurrence appears to be related to the age of the solution, i.e. the solution undergoes some form of degradation after a few hours. Another difficulty inherent in this method of fabrication is that of controlling resulting foil thicknesses. We finally decided in favour of another method based on one described by Ajitanand and Iyengar (Aj76).

A few mg of NE102 are dissolved in scintillation-grade xylene and the mixture allowed to stand for a few hours until all the NE102 has dissolved. A quantity of this solution is then transferred via a glass syringe onto the carefully cleaned and levelled face of a photomultiplier tube. In order to facilitate drying, the photomultiplier is placed in a dust-free alumunium chamber which is slowly evacuated. Slow evacuation is necessary to avoid bubbles and breakages in the resulting film. Figure 3.5 shows the arrangement that was used. A nylon ring was used to prevent the TFPS solution from running down the sides of the photo-tube.

Both the levelling and the cleaning procedures mentioned are of importance. The former ensures that the films that are produced are of uniform thickness while the latter ensures that the film does not contain "dead spots" owing to foreign particles embedded in the films. If the films are to be removed from the tube-face, it is necessary to coat the glass with a thin layer of water soluble detergent. This allows the films to be floated off the tube with ease. Films were stored either in beakers of water or between moist sheets of filter paper in petri dishes.

An added feature of this method of making the TFPS detector on the photo-tube is the ease with which the film can be tested, since no handling of the film is required and the optical coupling between the film and the tube is clearly very good. The foils were tested as follows: a collimated beam of fission fragments from a ^{252}Cf(sf) source was directed onto various regions of the film inside the evacuated chamber. Using the simple electronic signal processing chain (fig. 3.5) the resulting pulse height spectra were recorded on a multichannel analyser (MCA).

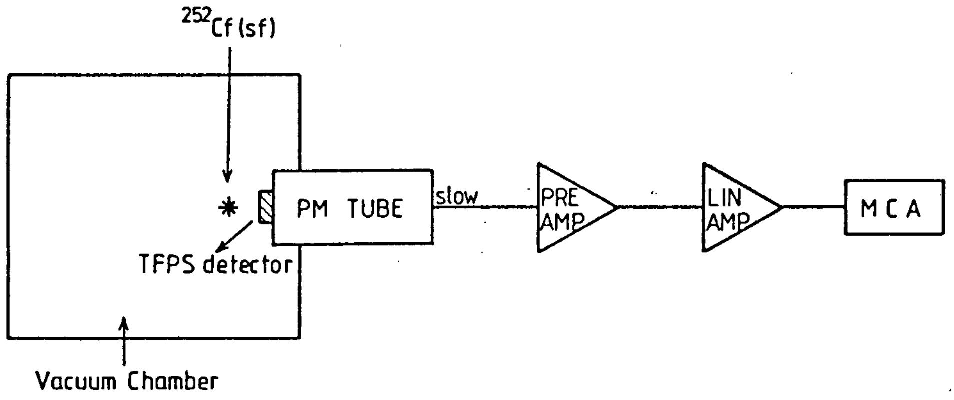

FIGURE 3.5 *Configuration used for testing TFPS detectors.*

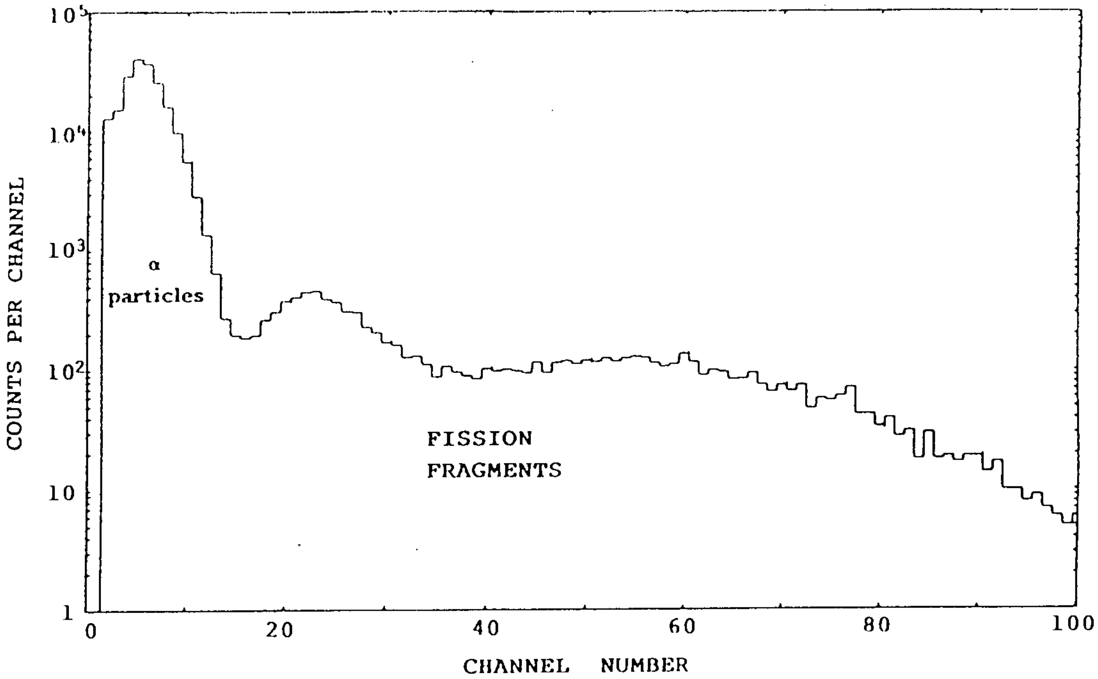

FIGURE 3.6A Scintillation pulse-height response from a 6μm thick TFPS detector irradiated with a ^{252}Cf(sf) source.

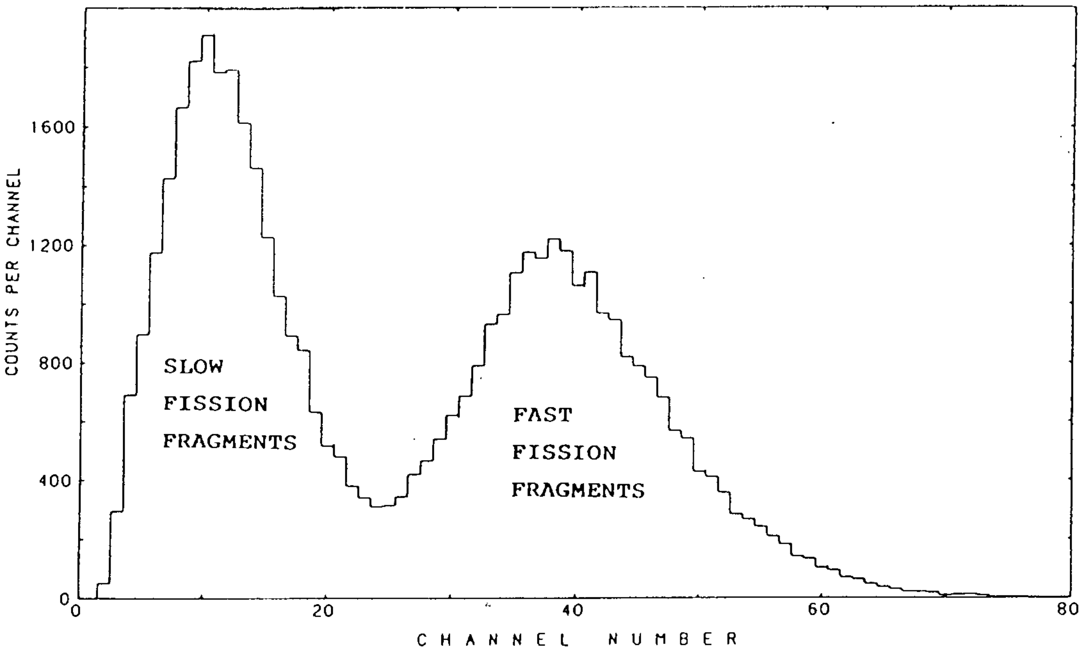

FIGURE 3.6B Scintillation pulse-height response from a 12 μm thick TFPS detector irradiated with a ^{252}Cf(sf) source. The alpha particles have been eliminated on the basis of pulse-height.

Experience and comparison with expected spectral features as reported in the literature allow us to distinguish between "good" and "bad" films. Interferometric methods in the forms of (i) Michelson's interferometer and (ii) Driver's method (Dr83) were used on a few films as an independent check on the uniformity and the thickness of the films. In all the cases that were tested both interferometric methods confirmed that the films were indeed uniform, as well as agreeing to within 10% of the calculated thicknesses. We show two pulse-height spectra which were obtained in the manner outlined. Figure 3.6A is plotted on a logarithmic scale and shows the spectrum from a TFPS detector 6 μm thick. We are able to identify three regions as (1)α-particles, (2) heavy (slow) fragments and (3) light (fast) fragments (Aj78, Mu70). In figure 3.6B, which was obtained from a 12 μm thick TFPS detector, the alpha group has been removed via pulse height discrimination.

3.2.5. Calibration of the TFPS detector.

In the wake of the reported linear velocity-dependent nature of the response of the TFPS detector to fission fragments a series of experiments was carried out with the aim of checking the linearity of the velocity response function and subsequently calibrating the TFPS detector.

A schematic diagram showing the experimental arrangement used is given in fig 3.7. The apparatus consists of an evacuated tube down which fission fragments are allowed to travel for a known distance. The time-of-flight over this distance is recorded and hence the fragment velocity determined. Since about 90% of the fission gamma rays having energy greater than 100 KeV are emitted

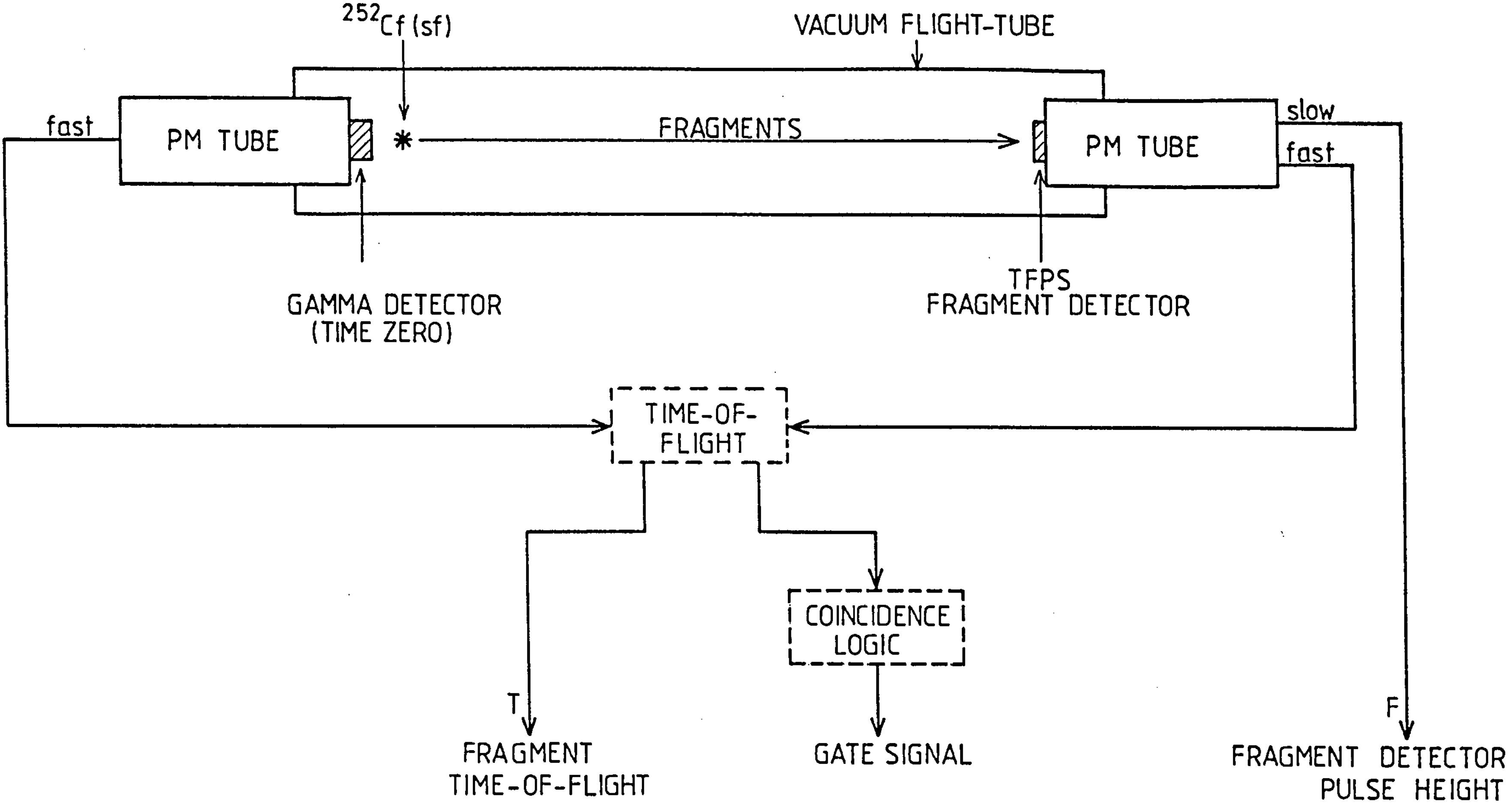

FIGURE 3. 7 *Schematic diagram of the electronic configuration employed to investigate the correlation between fragment velocity and TFPS detector pulse height. The time-of-flight method is used to measure fragment velocity.*

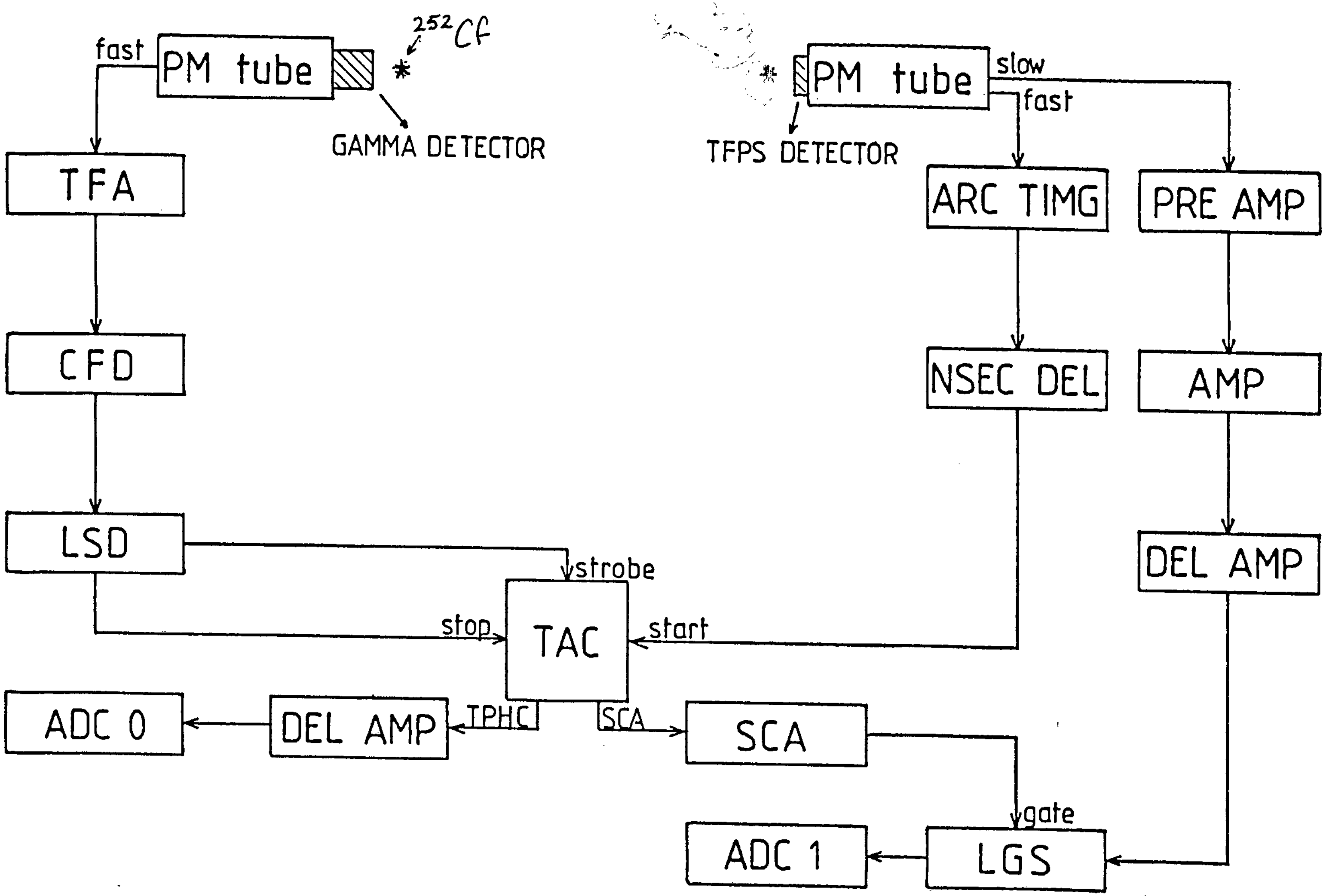

FIGURE 3.8 *Block diagram of the electronics used for the calibration of TFPS detectors.*

less than 1ns after scission (Sk70, Sk75); these prompt gamma rays provide a suitable time-zero signal for the time-of-flight measurements. The TFPS detector pulse-height for each detected fragment is recorded simultaneously. The detailed electronic configuration is shown in figure 3.8 from which it can be seen that the "logic" output from the TAC is used to gate the TFPS detector pulse-height. These time-of-flight versus pulse-height measurements were carried out for various different foil thicknesses. In figure 3.9 we show a two-parameter density plot of time-of-flight versus pulse-height for a 15 μm thick foil. It is evident from the graph that the two parameters are correlated with each other.

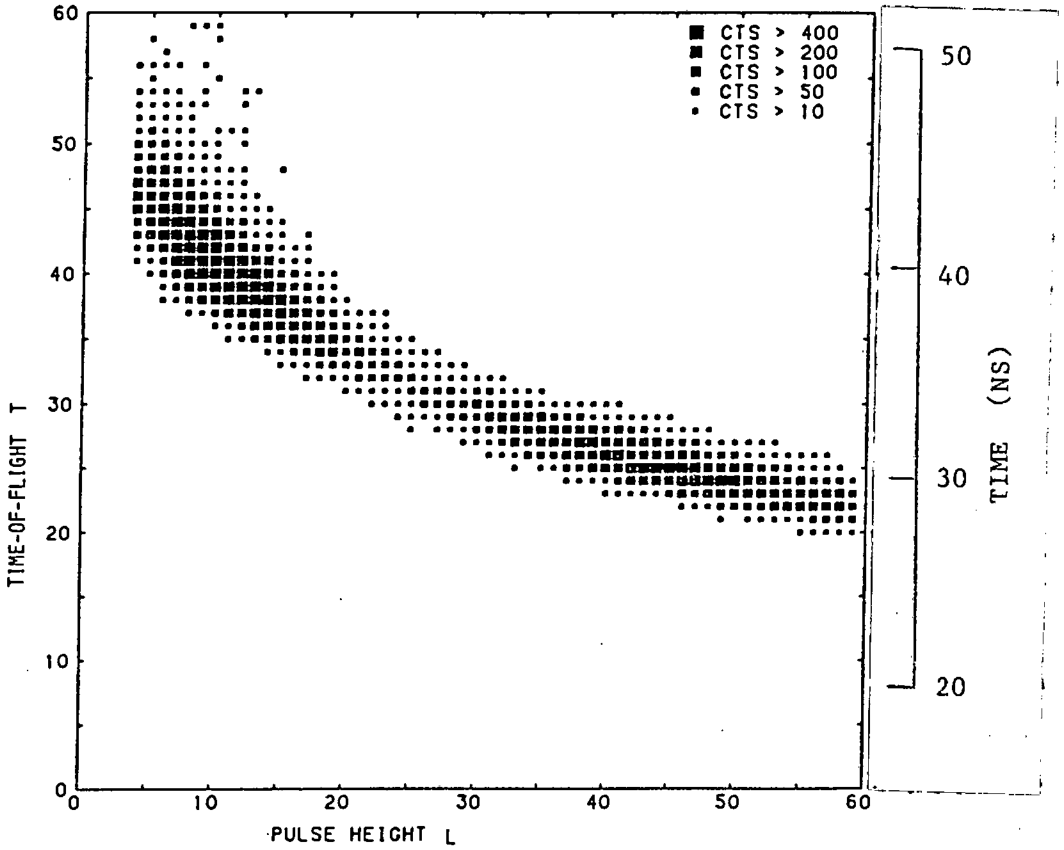

FIGURE 3.9 *Density plot of two-parameter spectrum, time-of-flight (i.e. velocity^{-1}) versus pulse height obtained using a ^{252}Cf fission fragment source and a 15 μm thick TFPS detector.*

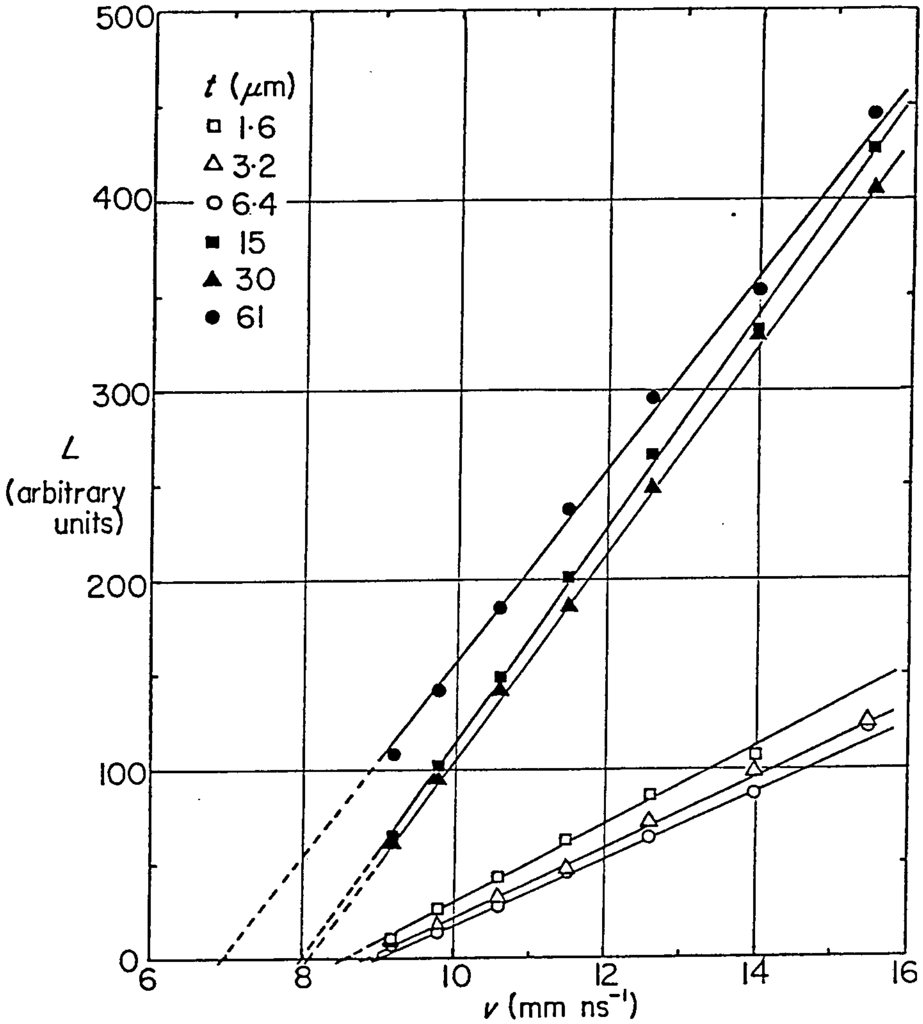

FIGURE 3.10 TFPS detector response, F, as a function of fragment velocity, V, for different detector thicknesses, t.

A detailed calibration yields the set of curves shown in figure 3.10. It is clear that the light output of the TFPS detector when exposed to fission fragments is proportional to the velocity of the incident fragment for the foils which were tested. This useful feature was put to use in measuring the neutron spectrum from ^{252}Cf (sf) in the restframe of the fission fragment as described in the following chapter.

4. CHAPTER FOUR: Results and discussion.

4.1. Outline of the analysis.

Reduction of the multiparameter data stored on buffer tape was carried out on the University of Cape Town's UNIVAC computer. The raw data consisted of a series of events each event comprising three parameters viz.,

(1) the neutron time-of-flight, T,
(2) the TFPS fragment detector pulse-height, F and
(3) the neutron detector pulse-height, L

The data were written to another tape in UNIVAC-word-compatible format so that each parameter occupied a 36-bit UNIVAC word. Subsets of the data were written to disk storage and analysed event-by-event. From the neutron time-of-flight the velocity in the laboratory frame of reference, v, was calculated. Hence, we were able to determine the energy, E, of each neutron in the laboratory frame of reference. In order to transform v to v_{PF} (the velocity of the neutron in the restframe of the forward fragment) the velocity of the forward fragment, V_F, was established from the F-pulse for the particular event. The appropriate vector subtraction yielded the velocity of the neutron in the fragment restframe. From this velocity we were able to calculate the energy in the fragment restframe, E_{PF}.

4.2. Presentation of the raw data.

Figures 4.1 show two-parameter plots of F versus T for the data collected at $\Theta_D=180°$. (See section 2.2.1 for the notation). The

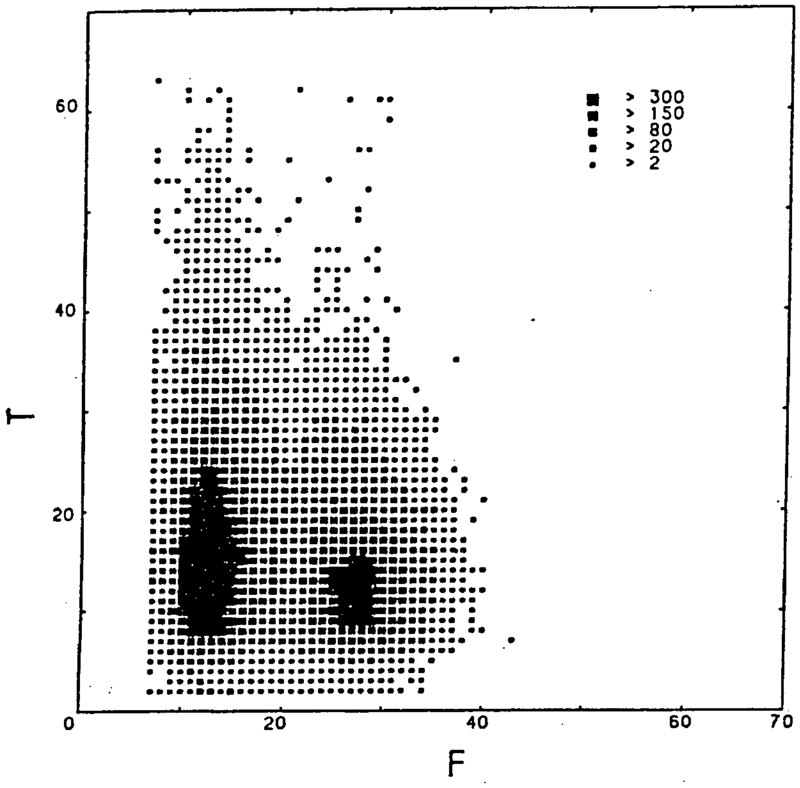

FIGURE 4.1(a) A plot indicating the density of events. The two-parameter spectrum shows the TFPS detector pulse-height, F, plotted against the neutron time-of-flight, T.

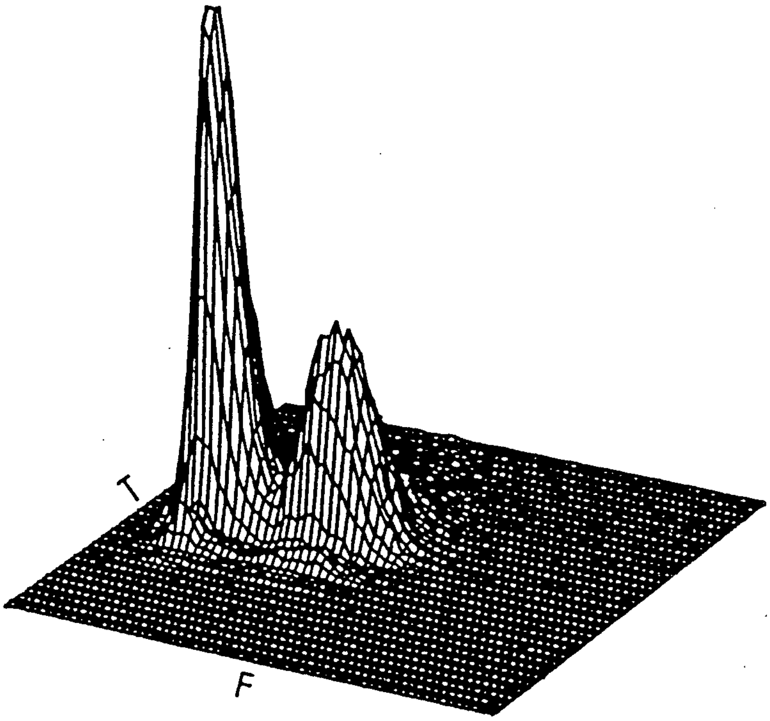

FIGURE 4.1(b) A 3-dimensional representation of event density showing TFPS detector pulse height, F, plotted against the neutron time-of-flight, T.

representation in figure 4.1(a) is that of a density plot while figure 4.1(b) is an isometric view. The projected F-spectrum and the projected T-spectrum are shown in figures 4.2(a) and 4.2(b), respectively. We note that the pulse-height distribution of figure 4.2(a) represents the distribution of backward fragments, since θ_D=180°. Thus, the three regions that are labelled, represent events associated with

A = slow backward fragments,

B = fast backward fragments and

C = symmetric and near-symmetric fission.

Now, since almost all the detected neutrons are emitted from the forward fragments, (section 2.2), it is convenient for the discussion to designate these regions in terms of the forward fragments. Hence,

A = *fast forward fragments and*

B = *slow forward fragments*

In figure 4.2(b) the small peak centred around zero nanoseconds is caused by gamma rays breaking through the pulse shape discrimination. This position corresponds to a flight time of 0.64nsecs, and hence it can be used to calculate the position of time-zero. A noteworthy feature of the spectrum is the low background which we can attribute to the use of (1) a low activity source in combination with the coincident detection of neutrons and fragments, (2) pulse-shape discrimination and (3) the boron-loaded liquid detector. Since even a neutron of very low energy will give rise to a signal which is equivalent to a 40keV electron, it is possible to use the detector at a bias setting which is just below this. In this way small signals including noise background are eliminated.

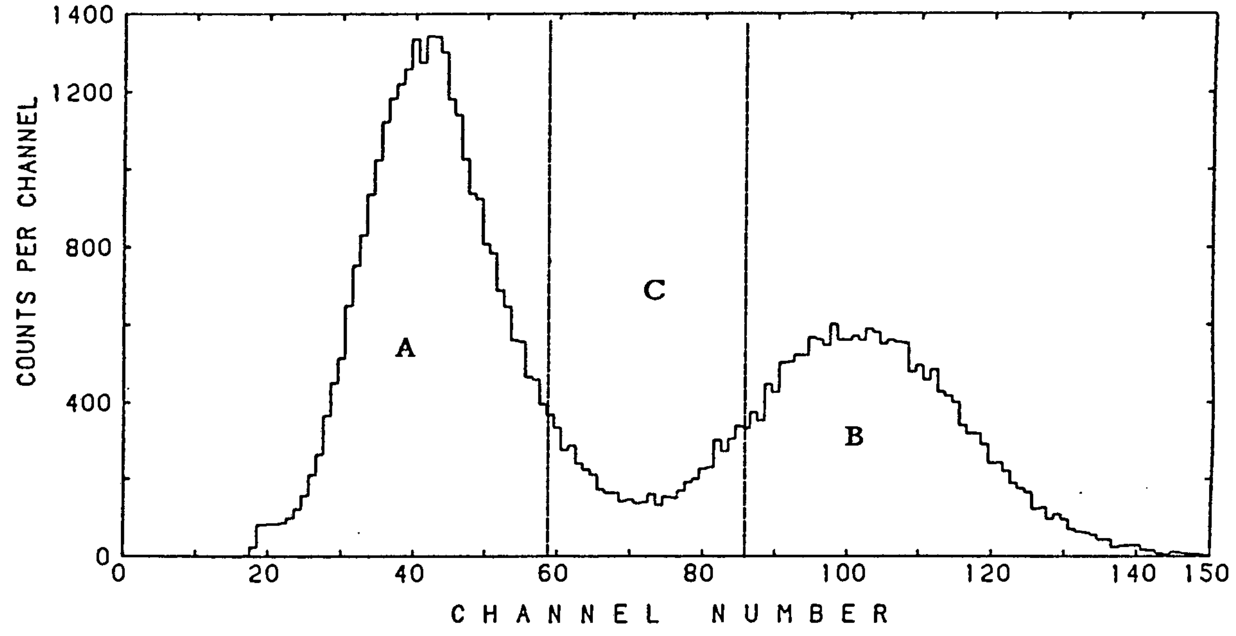

FIGURE 4.2(a) Pulse-height spectrum of fission fragments from ^{252}Cf (sf) recorded by a 12 μm thick TFPS detector. The regions A, B and C are used to identify the parent fragments of coincident neutrons as described in the text on page 4-3.

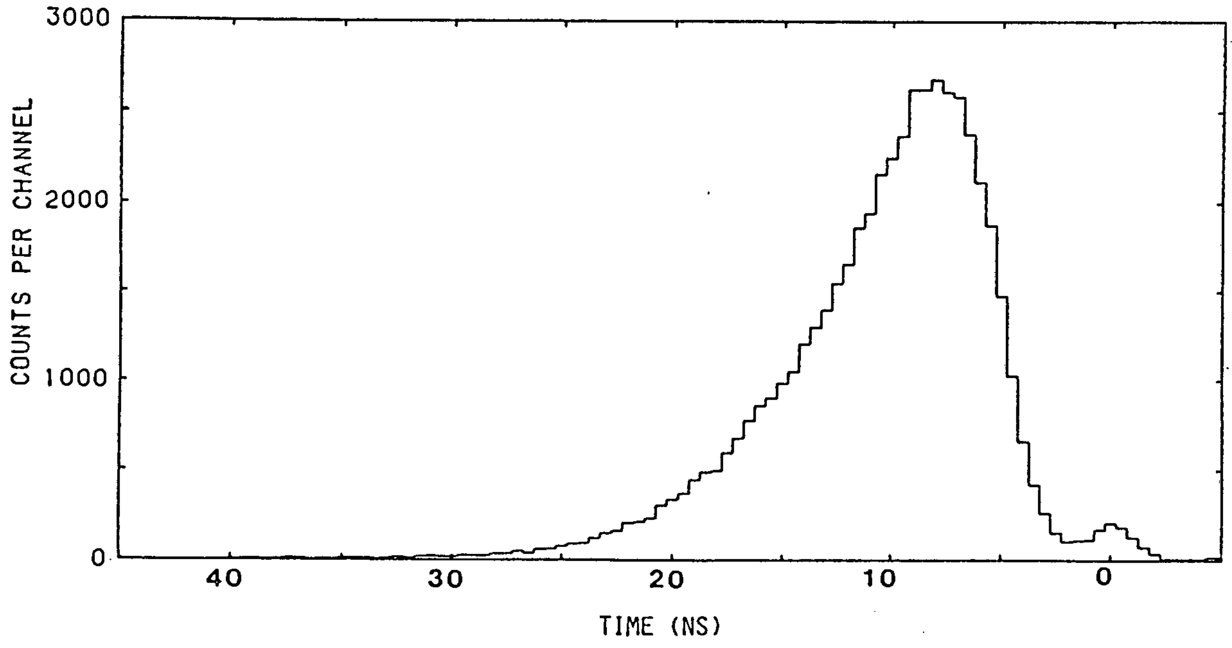

FIGURE 4.2(b) Time-of-flight spectrum of neutrons from ^{252}Cf (sf) using a neutron flight path of 193 mm. The small peak on the right is due to the tiny fraction of gamma rays which break through the pulse-shape discrimination.

Similar sets of data were obtained for $\Theta_D=90°$ and for $\Theta_D=130°$. The data collection times for each of the runs and the number of events that were collected per run are summarised in the table below.

Run	Θ_D	Time (hours)	events	events/min
A	180°	189.8	65280	5.8
B	130°	33.6	10540	5.2
C	90°	39.0	5780	2.4

4.2.1 Ratios

In order to investigate the influence of the fragment motion on the neutron spectrum more closely, we analyse the $\Theta_D=180°$ neutron spectra as a function of fragment mass (velocity) as follows.
The data were scanned to determine the time-of-flight spectra associated with each of the regions A, B and C of the F-spectrum. From these the fraction of neutrons associated with each of the three regions was calculated. The fractions were calculated as the ratios of the sub-spectra to the total neutron spectrum, respectively. The results, as a function of laboratory neutron energy, are shown in figure 4.3.

We find that more than 50% of the neutrons with energies greater than 2MeV are associated with region A of the F-sectrum while less than 40% of the neutrons in this energy range are associated with region B. Above 4MeV this preferential association with region A increases further so that there are almost twice as many neutrons

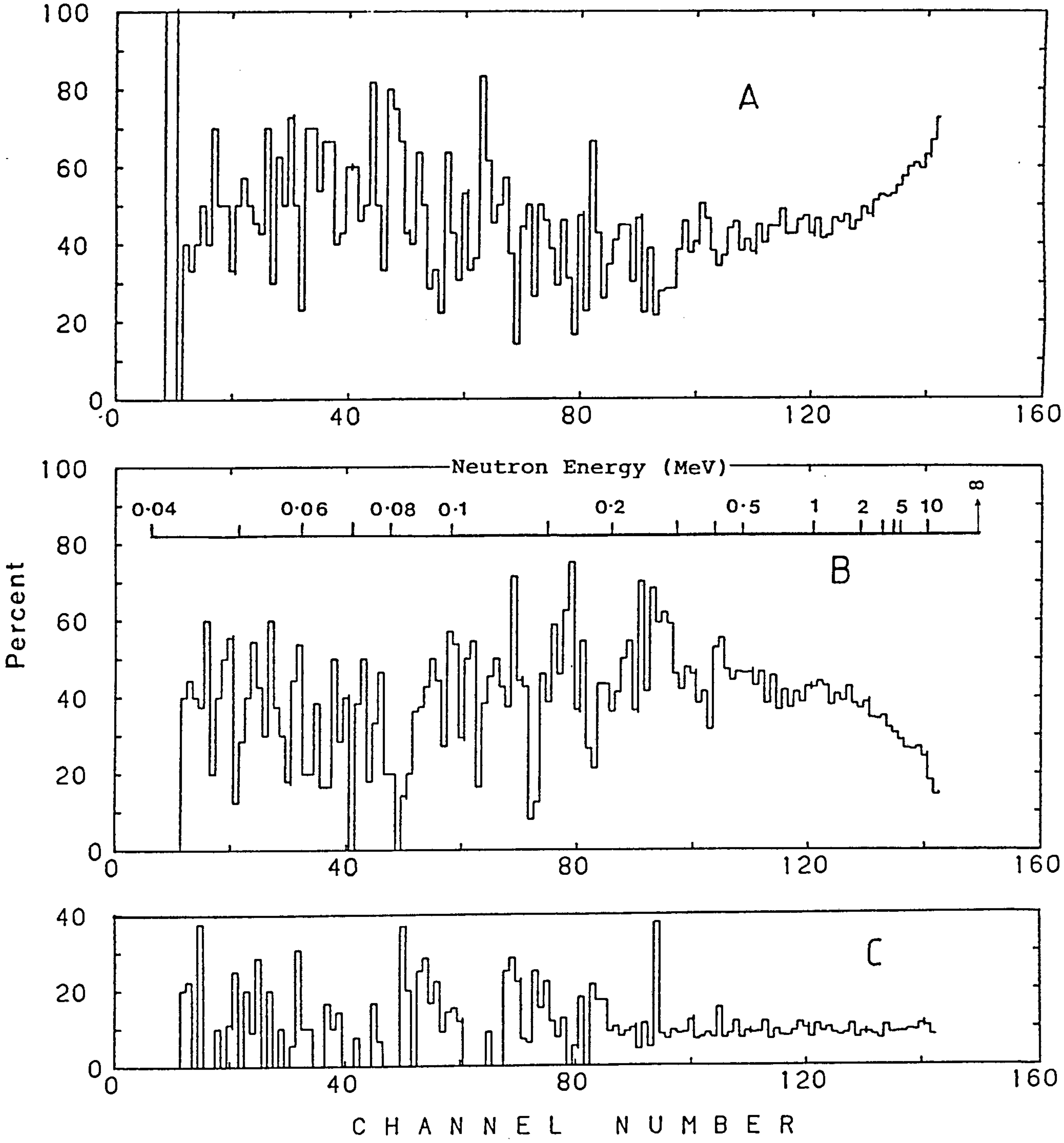

FIGURE 4.3 *Percentages of neutrons associated with the fast forward fragments (A), the slow forward fragments (B), and the undefined fragments (C), as a function of neutron energy (time-of-flight).*

associated with region A than with region B. We are able to understand this behaviour from the fact that the faster-moving fragments, A, contribute a higher translational velocity to the neutrons which they emit than do the slower-moving fragments, B. From a similar argument we would expect a higher proportion of low energy neutrons to be associated with the slow fragments. Such a trend is indeed observed in the energy region 0.2MeV to 0.4MeV. The neutrons associated with symmetric fission, region C, appear to be a random selection with respect to energy. The preferential association, ~60%, of the low energy neutrons, less than about 0.1MeV with region A is, however, contrary to the above trends. This is attributed to the finite range of Θ_D accepted. (See section 4.5.1 below)

4.3 The laboratory neutron energy spectrum

Before we proceed to detail the transformation of the neutron velocity measurements in the laboratory frame to that in the restframe of the fragment we show the energy spectrum of neutrons from ^{252}Cf (sf) in the laboratory frame, N(E), which was derived from our measurements. This was done by combining the data collected at each of the three Θ_D angles, viz., 180° 130° and 90°.

The velocity of each detected neutron in the laboratory frame of reference, v, was determined from the time-of-flight, T, parameter. Hence the energy of the neutron in the laboratory frame of reference, E, was calculated. An energy spectrum, N(E), was formed by suitable "binning" of each energy, event-by-event. In this way three spectra were determined, one at each of the afore-mentioned angles, respectively. The spectra, corrected for background, were combined taking into account (1) the different running times at each angle and (2) the relative geometries. The resulting spectrum was then corrected for the efficiency of detection of the NE321 boron-loaded liquid scintillator. (See section 3.1)

We show, in figure 4.4 the results of our measurement compared with the measurement of the neutron energy spectrum from ^{252}Cf (sf) in the laboratory frame performed by Green et al (Gr73). The data are plotted in the form, $\frac{\ln N(E)}{\sqrt{E}}$. (If the data are able to be represented perfectly by a Maxwellian this would yield a straight line. See Chapter 1). Our measurement extends over the range 0.2 MeV to 6 MeV. The latter limit is a result of the length of the flight path which limits the energy resolution.

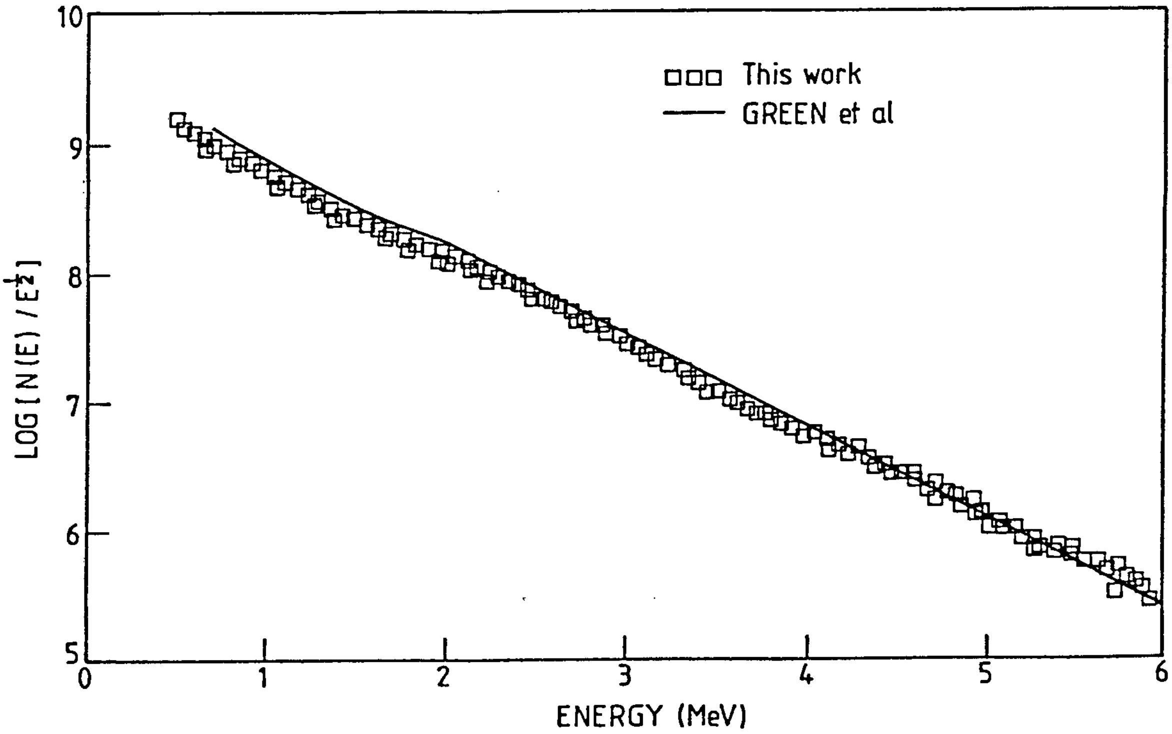

FIGURE 4.4 *Our measurement of the neutron energy spectrum in the laboratory frame for ^{252}Cf (sf) compared with the results of Green et al (Gr73).*

Our data are in reasonable agreement with that of Green et al. The differences indicated are a result of our method of measurement and poor statistics at the low energy end. However, our measurements extend beyond those of Green in the low energy region by about 300 keV. An experiment in which better averaging over all fragment directions occurs would yield much better results, as the number of Θ_D angles we have used is rather limited.

4.4. Transformation to the fragment restframe.

We describe in the subsequent paragraphs the steps that were required to transform v to v_{PF}. We also describe the various correcting factors that are necessary to apply to the resulting energy spectrum. (A flow diagram summarising the steps is shown in figure 4.9.)

4.4.1. Kinematics.

The relationship between the various velocity vectors is shown in figure 4.5. The neutron velocity in the laboratory frame, v, is the resultant of a vector addition involving the fragment velocity V_X, (X = F or B), and the velocity with which the neutron is emitted relative to the X-fragment, v_{PX}. Thus, if X=F then we have the following vector equation, viz.,

$$\vec{v} = \vec{V}_F + \vec{v}_{PF} \qquad (4.1)$$

The relationship between their magnitudes is given by

$$v = (V_F^2 + v_{PF}^2 - 2V_F v_{PF} \cos(180 - \Theta_P))^{\frac{1}{2}} \qquad (4.2)$$

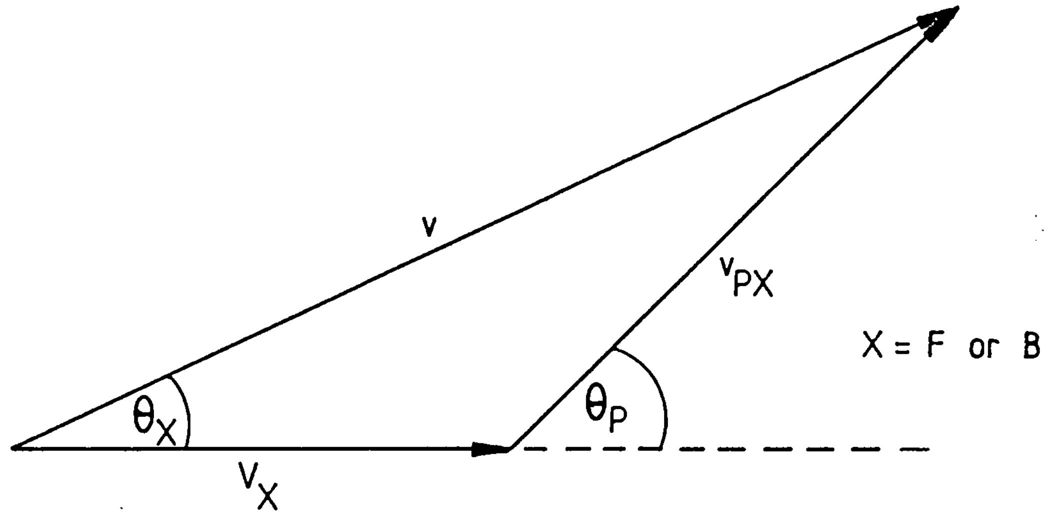

FIGURE 4.5 *Schematic illustration of the kinematics. The velocity of the neutron in the laboratory frame, v, is the resultant of the (parent) fragment velocity,* V_X *, and the velocity of the neutron in the restframe of the parent fragment.*

The vector addition simplifies in the ideal case where the neutron and the fragment that are detected are collinear. These special cases are shown in table 4.2.

Most of the events that were detected in our geometry, $\Theta_D=180°$, are of type-1 in the table. In order to minimise the percentage of events that would be incorrectly transformed by using equation 4.3 , only events in which v was greater than V_F were transformed. This selection criterion eliminated all events of the second type as well as a fraction of events of type-3. Our experiment deviates from the ideal situation owing to an angular spread in fragment direction that was recognised during the analysis. As the deviation of an individual fragment from $\Theta_F=0°$ cannot be ascertained, an estimate of the average spread was made. A correction, based on this estimate, was then applied to the results. (See section 4.5.1).

TABLE 4.2

Schematic	Neutron-fragment angle	Transformation equation
(1) 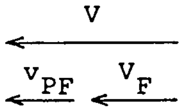	$\theta_F = 0°$	$v_{PF} = v - V_F$ (4.3)
(2) 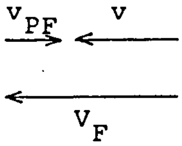	$\theta_F = 180°$	$v_{PF} = V_F - v$ (4.4)
(3) 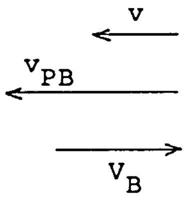	$\theta_B = 180°$	$v_{PB} = v + V_B$ (4.5)
(4) 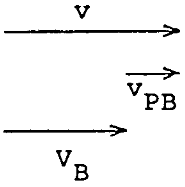	$\theta_B = 0°$	$v_{PB} = V_B - v$ (4.6) (neutron not detected)

The kinematic relationships simplify when the velocity vectors are collinear.

4.4.2. Determination of the forward fragment velocity.

The velocity of the backward fragment, V_B, was determined from the F-pulse by means of the calibration curves discussed in section 3.2.5. The forward fragment velocity, V_F, was then derived from V_B using Whetstone's curve of the fragment velocity as a function of the mass number of the fragment (Wh63) as well as the fact that for binary fission the sum of the two fragment masses M_F and M_B are related by the equation

$$M_F + M_B = 252 \qquad (4.7)$$

The curve of Whetstone is shown below in figure 4.6(a). In using this curve we are implicitly assuming that the total kinetic energy of the two fragments is always constant. This approximation introduces an average uncertainty of about 8% into the calculated value of v_{PF}. This figure of 8% is based on the width (full-width-at-half-maximum) of the total fragment kinetic energy distribution shown in figure 4.6(b).

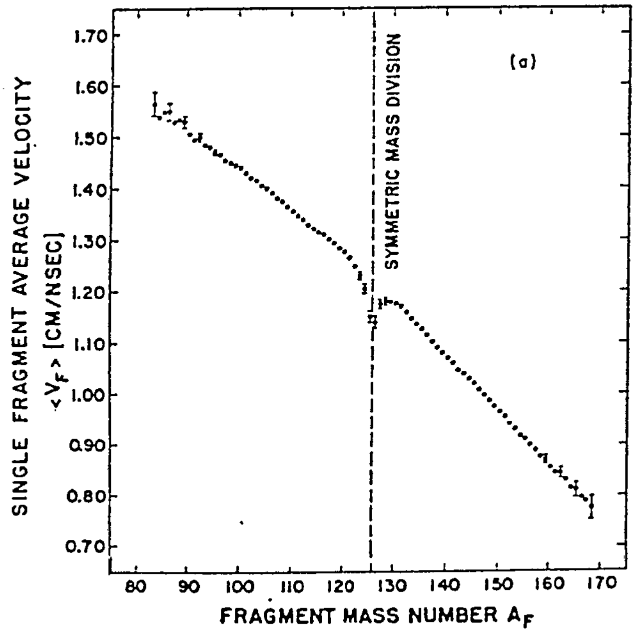

FIGURE 4.6(a)
The average velocity for single fragments emitted during spontaneous fission of ^{252}Cf plotted as a function of fragment mass. (Figure from Wh63)

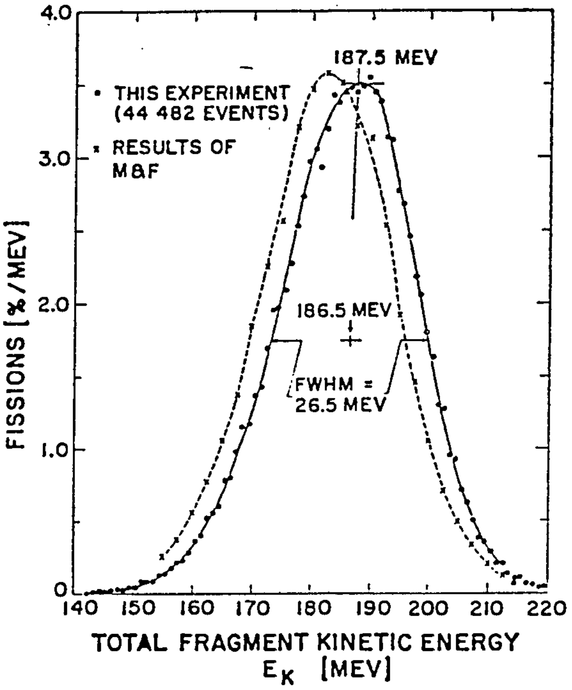

FIGURE 4.6(b)
The distribution of the total kinetic energy carried off by the fission fragments in $^{252}Cf(sf)$. (Figure from Wh63)

In figure 4.7(a) we present the velocity distribution for the forward fragments which were obtained as outlined. The maxima in the distribution correspond to the velocities 1.06cm/ns and 1.4 cm/ns, respectively. These values are in good agreement with other measurements (Wh63, Sc83) for the most probable slow and the most probable fast velocities for ^{252}Cf fission fragments. The number of events contained in each peak of the distribution is not the same owing to kinematic factors. However, we apply a correcting factor in the final energy spectrum. Figures 4.7(b) and 4.7(c) show two-parameter density plots in which V_F is plotted against the neutron velocity in the laboratory frame, v. The dotted line, (fig. 4.7(c)), indicates the limit below which events were rejected for transformation as we have outlined in the previous section.

4.4.3. Corrections to the transformed energy spectrum.

Each event was processed according to the flow-diagram shown in figure 4.8. The result of each such processed event is the energy of the neutron in the restframe of the parent fragment, E_{PF}. These energies were sorted into a series of "energy bins" to form an energy spectrum, $N(E_{PF})$. In order to correct the spectrum for the efficiency of neutron detection, (see section 3.1) a weight equal to the detector efficiency as a function of energy, $\varepsilon(E)$, was assigned to each neutron of laboratory energy, E. As we have pointed out in section 4.4.2 it is necessary to apply a correcting factor to the energy spectrum in which kinematic factors are taken into account. This kinematic correction factor depends on the motion of the fragment from which the neutron was emitted as well as on the solid angle of neutron detection. The solid angle of detection which is subtended by the neutron detector depends on

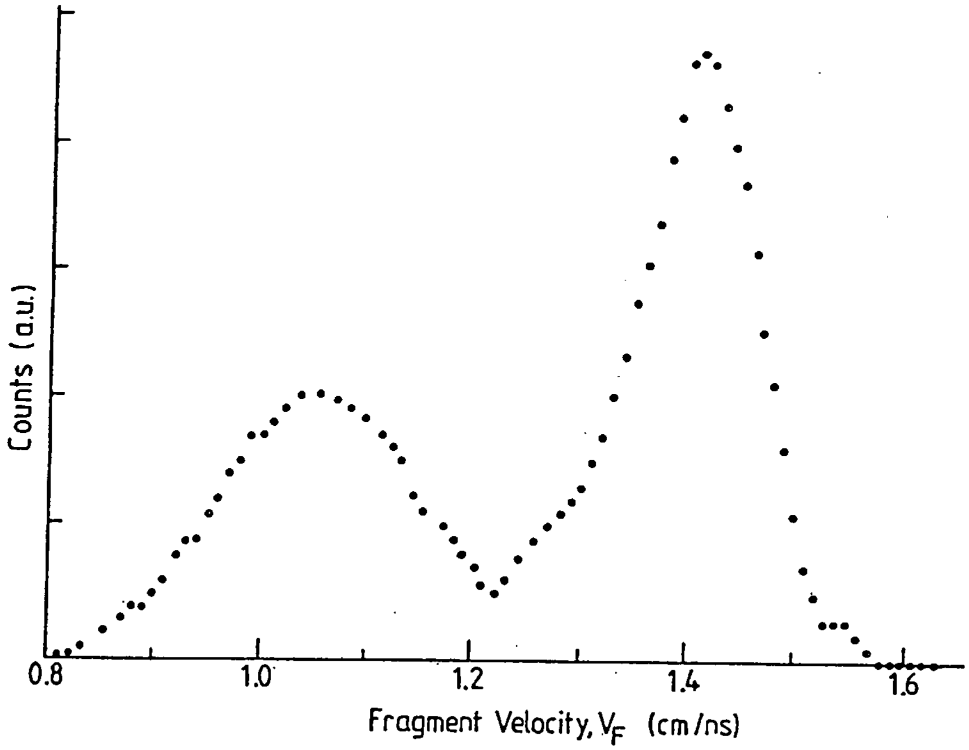

FIGURE 4.7(a) The velocity distribution of the forward fragments, from ^{252}Cf (sf). The forward fragment velocity, V_F is determined from a measurement of the velocity of the backward fragment, V_B.

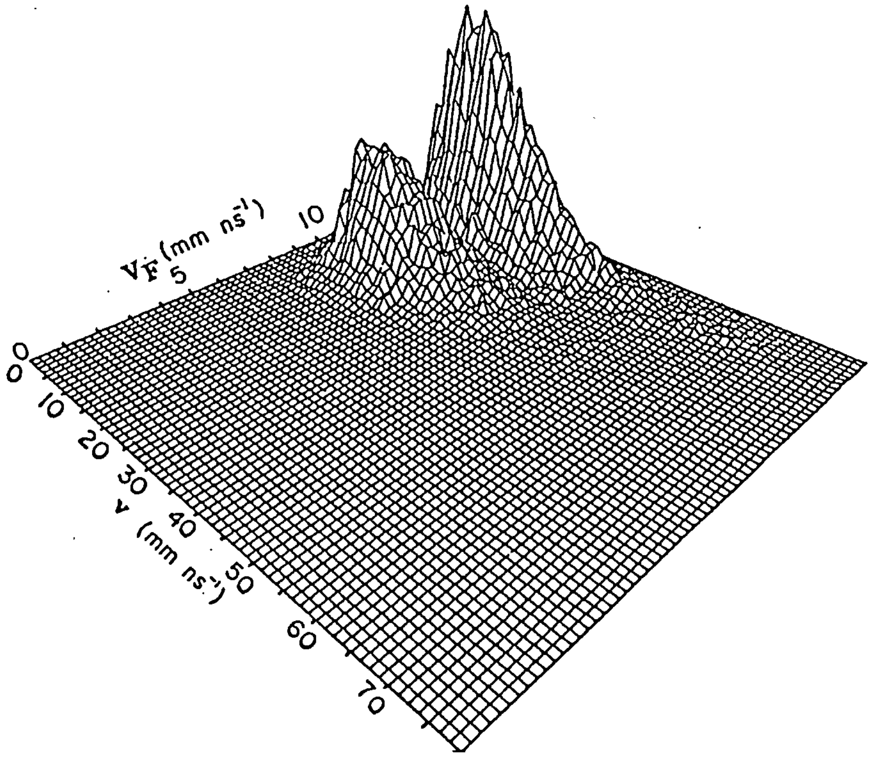

FIGURE 4.7(b) A 3-dimensional view of the density of events, showing a two-parameter plot of the forward fragment velocity V_F versus the neutron velocity in the laboratory frame, v.

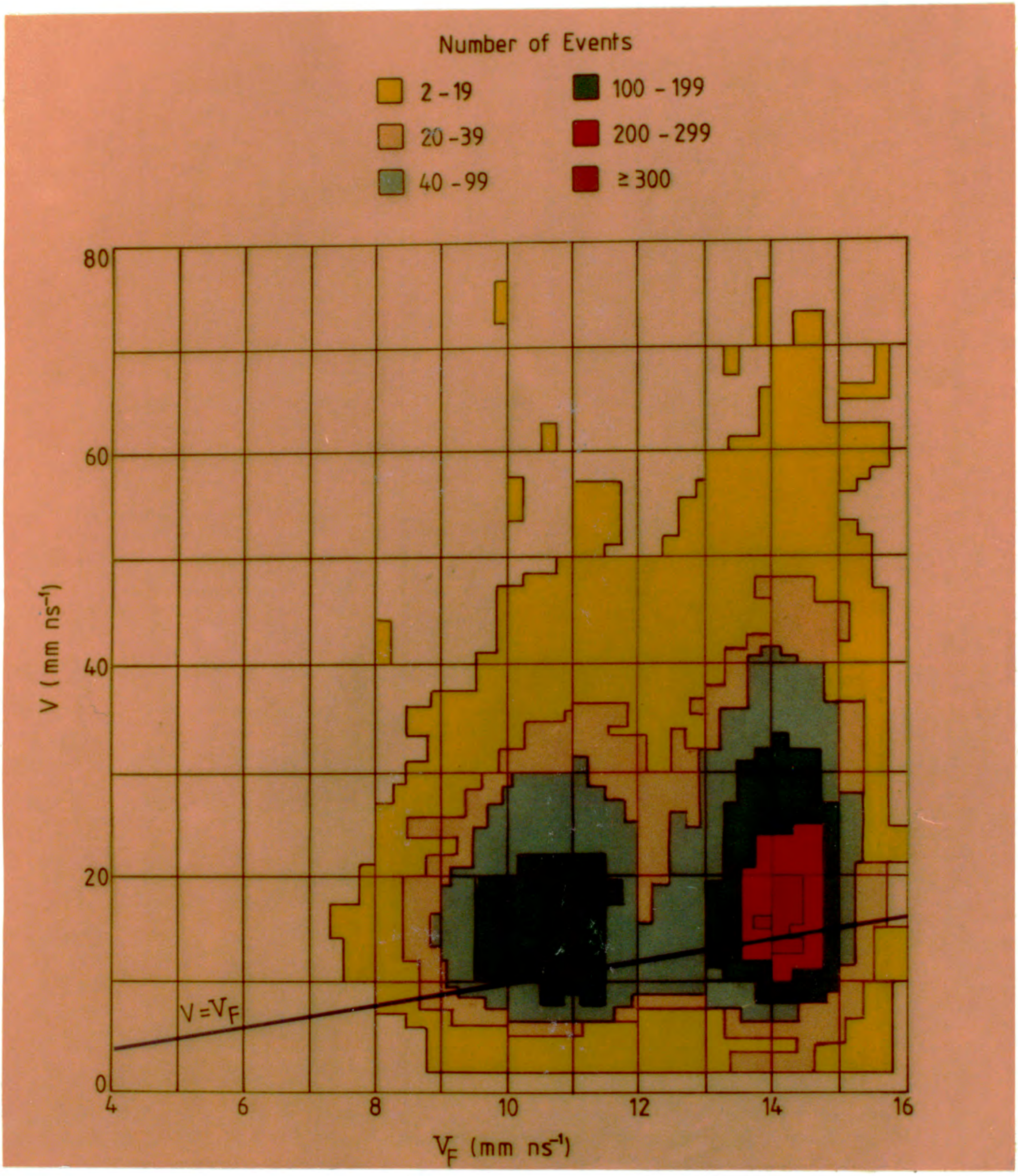

FIGURE 4.7(c) *A two-parameter density plot showing the forward fragment velocity V_F, plotted against the neutron velocity in the laboratory frame, v. The blue line represents the equation $v = V_F$. Only events above the line were processed according to the flow-diagram, figure 4.8.*

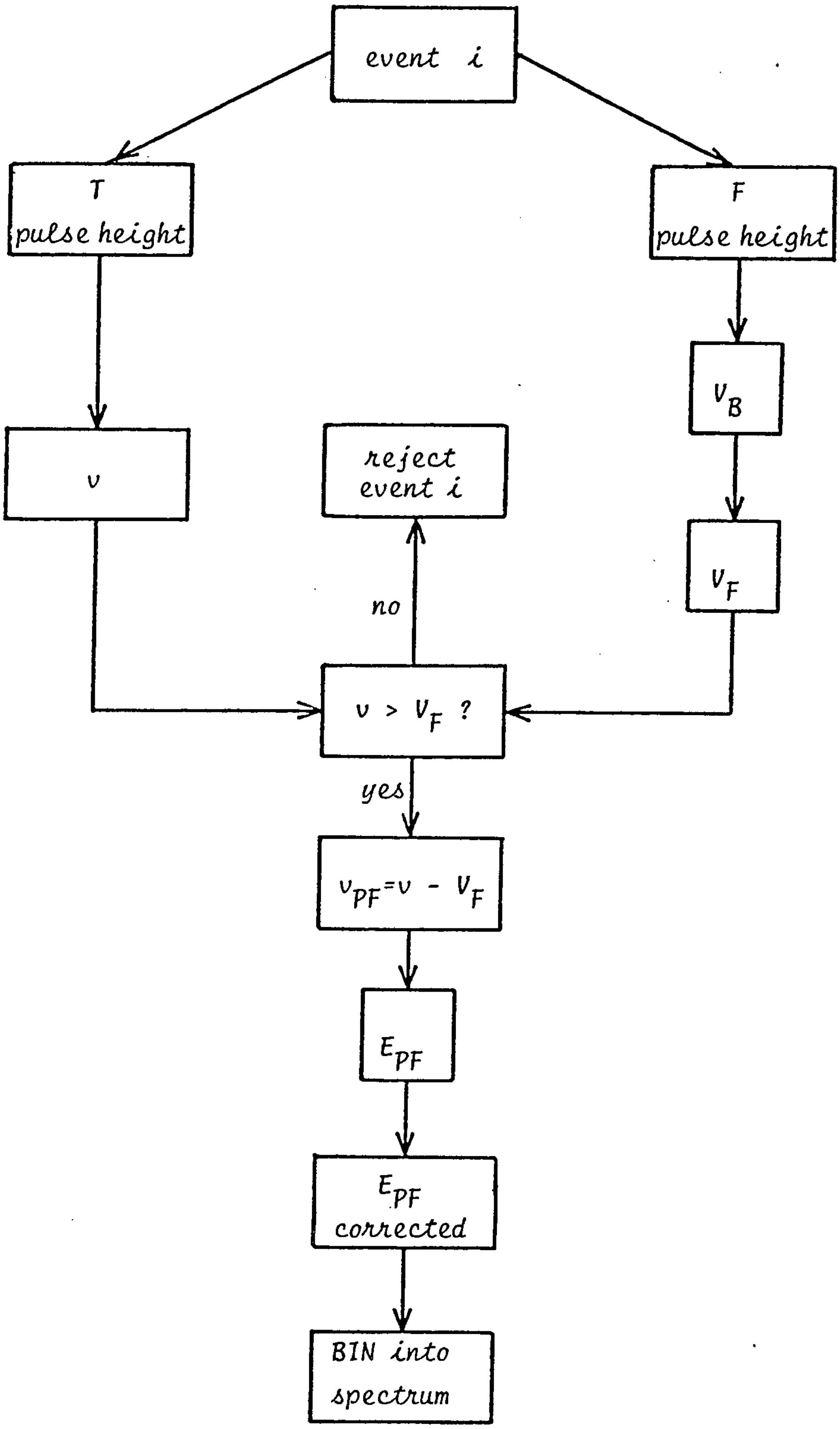

FIGURE 4.8 Simplified flow-diagram indicating the steps required to transform the neutron time-of-flight parameter, T, of event i to a energy in the restframe of the parent fragment of the neutron.

the kinematics as well as on the geometry. More specifically, the solid angle depends on

(1) the magnitudes of V_F and v_{PF} and

(2) the angle θ_P .

For a particular value of v_{PF} , emitted in a random direction with respect to the parent fragment, the probability that the resulting neutron trajectory will fall within the detection cone will increase as V_F increases. We, therefore, need to calculate the probability that a neutron of velocity, v_{PF}, will be detected given that it was emitted from a fragment of velocity V_F. Thus, each energy, E_{PF}, was assigned a weight calculated as a function of the kinematic parameters mentioned. (See Appendix A).

4.5. Results and discussion.

We present the results of these calculations in the figures below. In order to show the effect of some of the corrections to the spectrum, we show :

(1) the uncorrected spectrum, figure 4.9(a)

(2) the spectrum corrected for neutron detector efficiency and kinematic effects 4.9(b)

4.5.1. The angular spread of the fragments.

Before we proceed to compare our measurement of the spectrum of neutrons from ^{252}Cf(sf) in the restframe of the fragment with previous measurements we discuss the effects of the angular spread of the fragments in calculating the neutron spectrum in the restframe of the fragment. In figure 4.10 we show two sets of results representing the neutron energy spectrum in the restframe

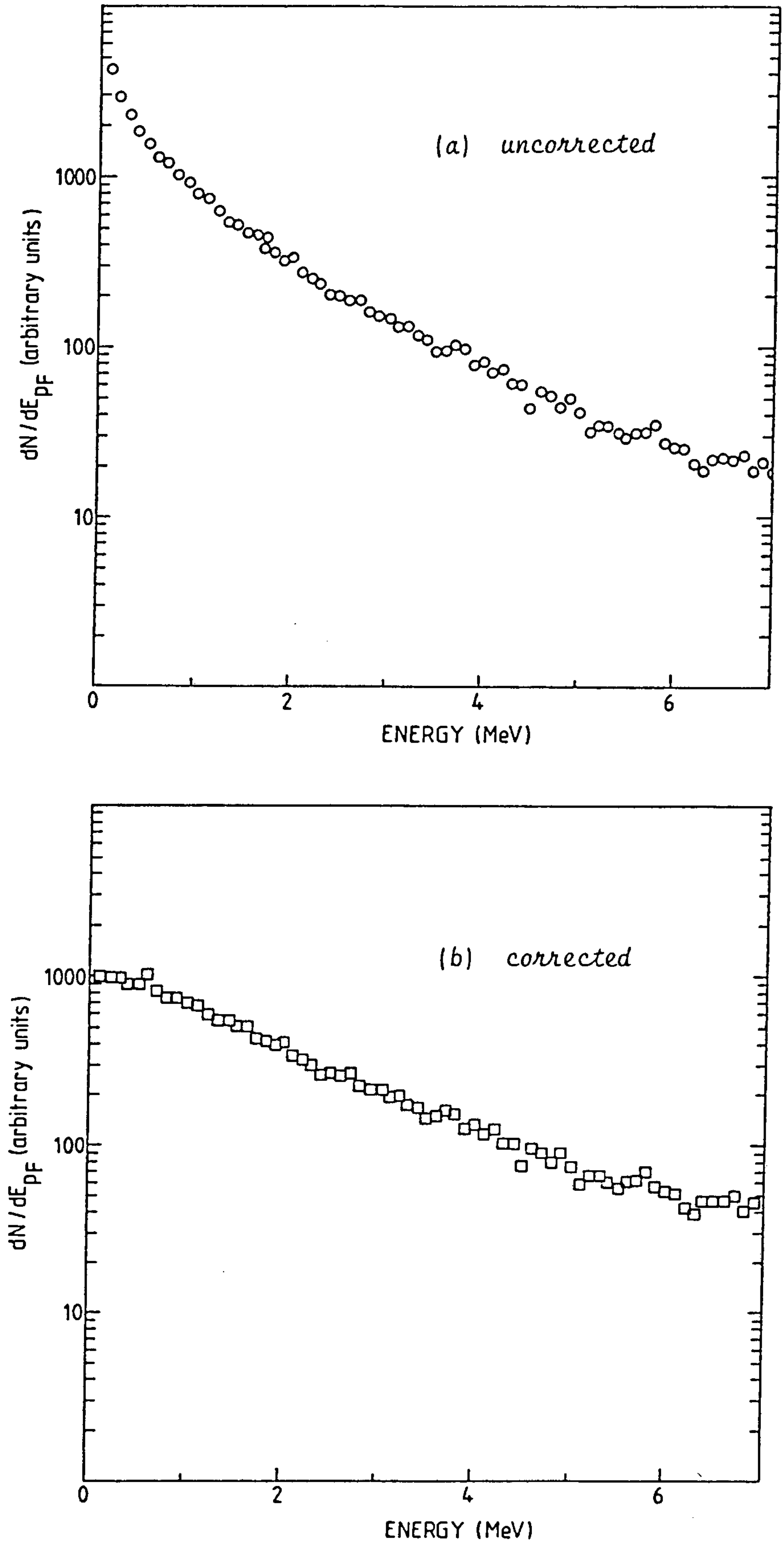

FIGURE 4.9 Logarithmic plot showing the energy spectrum of neutrons in the fragment restframe for ^{252}Cf (sf). The results shown in (a) have not been corrected for neutron detector efficiency and kinematic effects. The corrected spectrum is shown in (b).

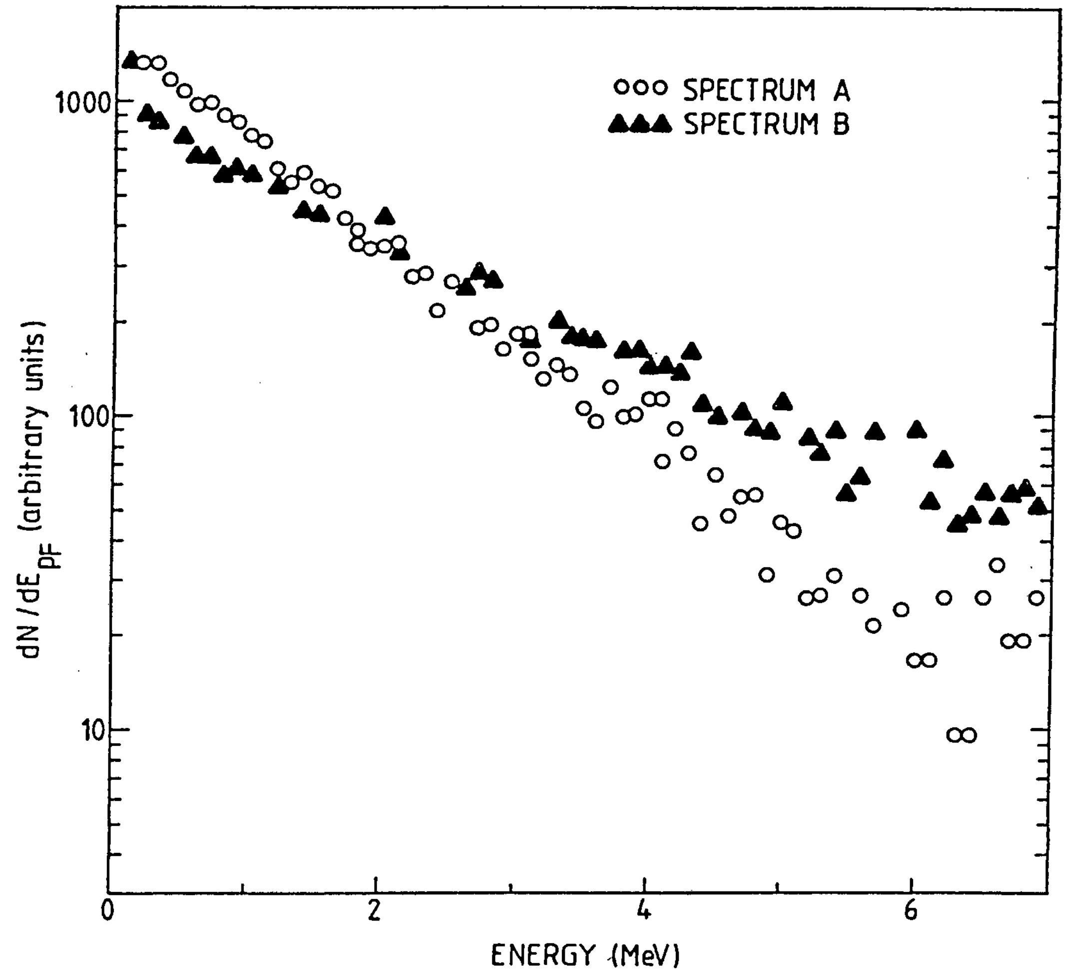

FIGURE 4.10 *Two sets of results for the measurement of the energy spectrum of neutrons in the restframe of the fragment for ^{252}Cf (sf). Spectrum A was derived by selecting only slow forward parent fragments, while spectrum B was derived by the selection of only fast forward parent fragments. The difference between the two spectra results from an angular spread of fragments away from Θ_F = 0°.*

of the fragment. In each case a different set of selection criteria has been placed on the parent fission fragment. Spectrum A was obtained by choosing only those events in which the parent (forward) fragment was a slow fragment. Spectrum B, on the other hand, was determined by selecting only the events associated with fast forward fragments. It is clear that the two sets of results differ markedly. We attribute this difference between our two sets of results to the angular spread of the fragments away from $\Theta_F = 0°$. This deviation affects the tranformation from v to v_{PF} in two ways:

(1) Since an estimate of the average angular spread, $<\Theta>$, was used to correct for the effect only a small fraction of the neutron velocities, v, are accurately transformed to v_{PF}. In most cases the correction is either too small or too large. This is demonstrated in the diagram below.

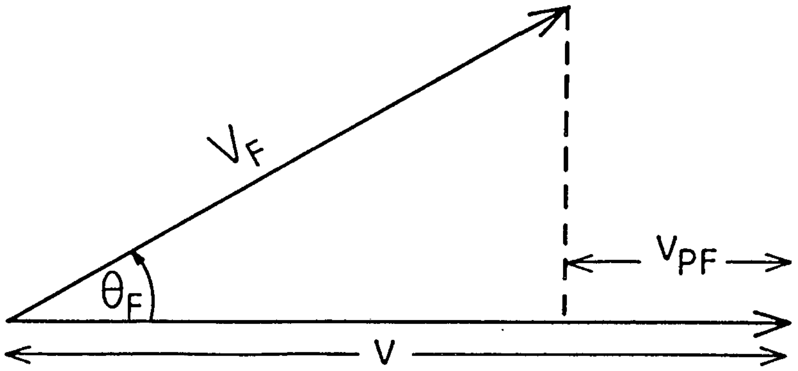

FIGURE 4.11 *The angle Θ_F is not known for each individual event. An estimation of the average spread $<\Theta>$ is thus made for all events. If $<\Theta>$ is larger (smaller) than Θ_F in a particular case then the value calculated for v_{Pf} is smaller (larger) than its true value.*

From this sketch the relevant quantities are seen to be related as follows:

$$v_{PF}=v-V_F\cos\Theta_F \qquad (4.8)$$

The angle Θ_F is, however, not known. We, therefore, estimate an average angular spread, $<\Theta>$. Thus, the value that is calculated for v_{PF} will exceed the true value of v_{PF} if Θ_F is in fact smaller than $<\Theta>$. Similarly, the calculated value of v_{PF} will be underestimated if $<\Theta>$ is larger than Θ_F. In this latter case the error that occurs is calculated to vary between 0% and 10%. In the former case the error that occurs is somewhat smaller and can be expected to vary between 0% and 4%. A fraction of neutrons which have velocities, v, close to their parent fragment velocities will not be included in the final spectrum, since it can be seen from the equation above that if Θ_F is underestimated v_{PF} could be negative and hence the event will be rejected. It is difficult to estimate this fraction as it is dependent on the shape of the neutron spectrum in the restframe of the fragment!

(2) The second way in which the angular spread of the fragments affects our results is that a fraction of neutrons that originate from the backward fragment can now reach the neutron detector. This fraction is a function of the fragment velocity, since a fast backward fragment will pull neutrons out of the forward hemisphere more effectively than a slow backward fragment. Bowman et al (Bo63) have calculated the fraction of neutrons that are emitted into the forward hemisphere by a backward fragment as a function of fragment velocity. See figure 4.12.

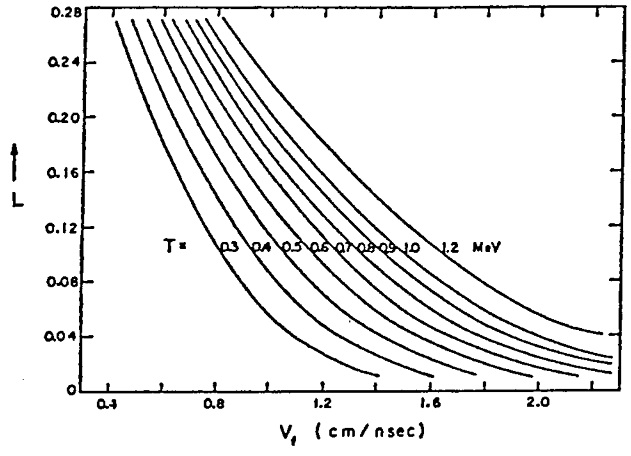

FIGURE 4.12
Fraction of neutrons L, going into the forward hemisphere in the laboratory system as a function of the temperature of the spectrum and the fragment velocity. (Figure from Bo63)

From these curves it is clear that, for a given nuclear temperature, T, the fraction of neutrons that goes into the forward hemisphere increases as the velocity of the backward parent fragment decreases. This trend is in keeping with our results. In deriving spectrum A i.e. slow forward parent fragments are selected, about 18% of the detected neutrons were found to have velocities, v, which were smaller than $V_F\cos\langle\Theta\rangle$. These slow forward fragments are ,of course, complementary to the fast backward fragments. In the case of spectrum B, which is associated with the slow backward fragments, a higher fraction, about 28%, of the neutrons had laboratory velocities which were smaller than $V_F\cos\langle\Theta\rangle$. (We note, however, that these percentages include the neutrons that are lost to the spectrum in the manner described above.) Hence, we expect the overall error in spectrum A to be smaller than that in spectrum B. We thus regard spectrum A to be a more accurate measurement of the neutron energy spectrum in the restframe of the fragment than the results indicated by either spectrum B or by the spectrum obtained when no restrictions are placed on the type of parent fragment, figure 4.9(b).

4.5.2. Comparison with previous measurement.

In figure 4.13 we compare our measurement for the neutron energy spectrum in the restframe of the fragment, spectrum A, in figure 4.10, with the following:

(a) the measurements derived from the work of Bowman (Bo63) and

(b) the predictions of the simple form of the evaporation model

The solid line in the diagram indicates the results of Bowman et al. The dashed line was calculated from the equation below, (see section 1.3), for an average spectral energy, $<E_{PF}>$, of 1.3 MeV (Bo63, Kl68). The spectra are normalised at an energy of 1.3MeV, this being the expected average energy of a Maxwellian fit to this spectrum.

$$N(E_{PF}) = \frac{4\,E_{PF}}{<E_{PF}>^2} \; exp \; \left(\frac{-2\,E_{PF}}{<E_{PF}>} \right) \qquad (4.9)$$

Our results are in broad agreement with those of Bowman across most of the energy range shown. The largest deviation is seen to occur at the low enery part of the spectrum, below 0.25MeV. Here, our measurements indicate 60% more neutrons than found by Bowman. However, in view of the largely unknown quantitative effect of the angular spread of the fragments, especially at these low energies we are not able to draw any physical conclusions. We note, however, that in tests where the data were analysed assuming a much larger value for $<\Theta>$ the results that were obtained followed the trends of Bowman's measurement at these energies. However, this was done at the expense of much poorer agreement at the higher energies.

Both our data and that of Bowman show systematic deviations from the predictions of the evaporation model. It is evident from this

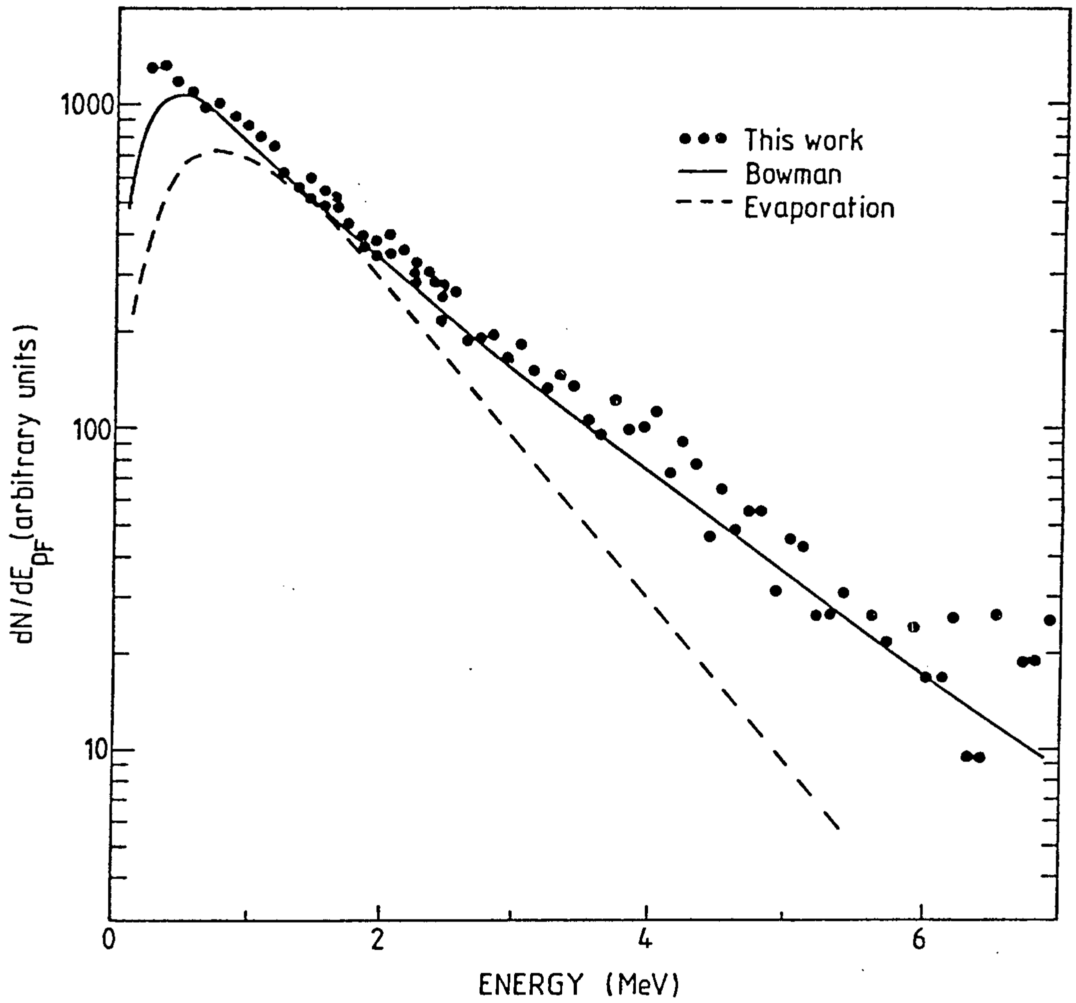

FIGURE 4.13 *The neutron spectrum in the fragment restframe for spontaneous fission of ^{252}Cf. Our measurement is compared here with the work of Bowman et al (Bo62, Bo63). The dashed line indicates the predictions of simple evaporation theory. Data and calculation are normalised to 530 units at 1.3 MeV.*

direct comparison between theory and experiment that simple evaporation theory is not able to explain the neutron spectrum adequately. Bowman et al have indicated that a good phenomenological fit to their data can be made by superposing three evaporation spectra each with a different average energy. (See equation 1.5).

4.5.3. Conclusions and further work.

In this work we have demonstrated the viability of a new method of determining the neutron spectrum of ^{252}Cf(sf) in the restframe of the fission fragment using a thin film plastic scintillator to measure the fragment velocity. Our results agree with those of earlier measurements over a good portion of the energy range. However, it is clear, that the directions of the fission fragments have to be more accurately monitored in future experiments. A change to the design of the experiment is envisaged which would yield more accurate results: in the current configuration the velocity of the forward fragment is obtained by performing a measurement on the backward fragment. In the worst possible case this can introduce an error of 20% into the value obtained for the forward fragment velocity. In order to measure the forward fragment velocity directly a TFPS detector in transmission geometry can be used. However, care needs to taken as regards the design of the light guide that is required. This has been shown by Gujrati and Lessard (Gu83) to be an extremely important factor in determining the response of the detector.

Although a neutron detector of larger diameter would increase the count-rate, thus improving the statistical accuracy of the data, the angular resolution will suffer as result. A thicker detector, on the other hand, will require a longer flight path in order not to increase the uncertainty in this measurement. If we wish, thus, to obtain good statistical accuracy without having to have extrememly long running times it is necessary to determine accurately the fragment trajectory in any direction rather than to collimate the source very tightly. This will, of course, necessitate the use of a position-sensitive detector. However, the degree of ambiguity in assigning a parent fragment will increase as Θ_F increases. Hence, the analysis of the data will not be as straight-forward as in the case where $\Theta_F = 0°$. One way of maintaining the spirit of our present experiment would be to use a ^{252}Cf source with a large surface area. This source can then be fitted with a collimator of design as shown below. Only fragments which are emitted parallel to the tubes will thus be selected. In this way all the fragments that are detected will have a well-defined direction while the count-rate will also be increased. In addition, no major modifications have to be made to the current configuration apart from performing a direct measurement of the velocity of the forward fragment.

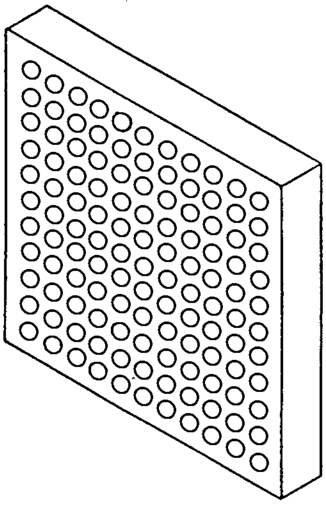

FIGURE 4.14
Collimator grid selects fission fragments in well-defined direction (to within ± 5°)

REFERENCES

Ad78 : J.M. Adams and G. White, Nucl. Instrum. Methods 156 (1978) 459

Aj76 : N.N. Ajitanand and K.N. Iyengar, Nucl. Instrum. Methods 133 (1976) 71

Aj77 : N.N. Ajitanand, Nucl. Instrum. Methods 143 (1977) 345

Aj78 : N.N. Ajitanand, K.N. Iyengar and S.R.S. Murthy, Phys. Rev. 18 (1978) 1745

Aj82 : N.N. Ajitanand, K.N. Iyengar and S.R.S. Murthy, Nucl. Instrum. Methods 193 (1982) 587

Ba75 : R.K. Batra and A.C. Shotter, Nucl. Instrum. Methods 124 (1975) 101

Be83 : G. Bendiscioli, V. Filippini, G. Fumagalli, E. Lodi Rizzini, C. Marciano, C. Milani, A. Rotondi and A. Venaglioni, Nucl. Instrum. Methods 206 (1983) 471

Bj80 : S. Bjornholm and J.E. Lynn, Rev. Mod. Phys. 52 4 (1980) 725

Bl54 : J.M. Blatt and V.F. Weisskopf, Theoretical Nuclear Physics, John Wiley and Sons, New York (1952)

Bl73 : M.V. Blinov, N.M. Kazarinov and I.T. Krisyuk, Sov. J. Nucl. Phys. 16 (1973) 1115

Bo39 : N. Bohr and J.A. Wheeler, Phys. Rev. 56 (1939) 426

Bo57 : L.M. Bollinger and G.E. Thomas, Rev. Sc. Instrum. 28 (1957) 489

Bo62a : H.R. Bowmann, S.G. Thompson, J.C.D. Milton and W.J. Swiatecki, Phys. Rev. 126 (1962) 2120

Bo62b : D. Bodansky, Ann. Rev. Nucl. Sci. 12 (1962) 79

Bo63 : H.R. Bowman, J.C.D. Milton, S.G. Thompson and W.J. Swiatecki, Phys. Rev. 129 (1963) 2133

Bo79 : J.W. Boldeman, D. Culley and R.J. Cowley, Trans. Am. Soc. 32 (1979) 733

Br59 : F.D. Brooks, Nucl. Instrum. Methods 4 (1959) 151

Br74 : P. Braun-Munzinger and C.K. Gelbke, Nucl. Instrum. Methods 114 (1974) 141

Dr83 : H.S.T. Driver, University of Cape Town, unpublished

Fe75 : N. Feather and D.G. Vass, Comm. Royal Soc. of Edin. (Phys. Sci.) 4 (1975) 47

Fr39a : D.R. Frisch and L. Meitner, Nature (London) 143 (1939) 239

Fr39b : J. Frenkel, Phys. Rev. 55 (1939) 987

Fr52 : J.S. Fraser, Phys. Rev. 88 (1952) 536

Fr66 : J.S. Fraser and J.C.D. Milton, Ann. Rev. Nucl. Sci. 16 (1966) 379

Fu62 : R.W. Fuller, Phys. Rev. 126 (1962) 684

Ge71 : C.K. Gelbke, K.D. Hildenbrand and R. Bock, Nucl. Instrum. Methods 95 (1971) 397

Ge77 : H. Geissel, K. Guttner, S. Hofmann and G. Munzenberg, Nucl. Instrum. Methods 144 (1977) 456

Gl65 : L.E. Glendenin, J.P. Unik and H.C. Griffin, Proc. of IAEA Symp. on Phys. and Chem. of Fission, 1 (1965) 377

Go74 : P.D. Goldstone, R.E. Malmin, F. Hopkins and P. Paul, Nucl. Instrum. Methods 121 (1974) 353

Gr73 : L. Green, J.A. Mitchell and N.M. Steen, Nucl. Sci. Eng. 50 (1973) 257

Gu83 : Gujrathi and L. Lessard, Nucl. Instrum. Methods 206 (1983) 183

Ha39 : O. Hahn and F. Strassmann, Die Naturwissenschaften, 27 (1939) 11

Hi56 : D.L. Hill and J.A. Wheeler, Phys. Rev. 103 (1956) 1292

Hy64 : E.K. Hyde, The Nucl. Prop. of Heavy Elem., 3 (1964)

Ja65 : M.E. Jackson and G.E. Thomas, Rev. Sci. Instrum. 36 (1965) 419

Je71 : L. Jeki, Gy. Kluge, A. Lajtai, P.P. Dyachenko, B.D. Kuzkinov, Prompt Fiss. Neutr. Spec. (Proc. Cons. Meeting, IAEA, Vienna) (1972) 81

Ke78 : K. Ettling and W. von Witsch, Nucl. Instrum. Methods 148 (1977) 299

Kl71 : Gy. Kluge. Phys. Lett. 37B (1971) 217

Kn79 : G.F. Knoll, Radiation Detection and Measurement, John Wiley and Sons, USA (1977)

Ko75 : J.W. Kohl, Nucl. Instrum. Methods 125 (1975) 413

Ma68 : J.B. Marion and F.C. Young, Nuclear Reaction Analysis, North Holland Pub., Amsterdam (1968)

Ma82 : D.G. Madland and J.R. Nix, Nucl. Sci and Eng. 81 (1982) 213

Mc74 : W.J. McDonald, A.I. Kilvington, C.J. Batty and J.L. Weil, Nucl. Instrum. Methods 115 (1974) 185

Me67 : J.W. Meadows, Phys. Rev. 157 (1967) 1067

Mu70 : M.L. Muga, D.J. Burnsed, W.E. Steeger and H.W. Taylor, Nucl. Instrum. Methods 83 (1970) 135

Mu71 : M.L. Muga, Nucl. Instrum. Methods 95 (1971) 349

Mu72 : M.L. Muga, D.J. Burnsed and W.E. Steeger, Nucl. Instrum. Methods 104 (1972) 605

Mu73a : L. Muga and G. Griffith, Nucl. Instrum. Methods 109 (1973) 289

Mu73b : L. Muga, A. Clem and G. Griffith, Phys. and Chem. of Fiss. 2 (1973) 451

Mu73c : M.L. Muga and G.L. Griffith, Nucl. Instrum. Methods 3 (1973) 581

Mu74 : L. Muga and M. Diksic, Nucl. Instrum. Methods 122 (1974) 553

Mu75 : L. Muga, Nucl. Instrum. Methods 124 (1975) 541

Ni74 : H. Nifenecker, C. Signarbieux, R. Babinet and J. Poitou, Phys. and Chem. of Fiss. (Proc. Symp. Rochester, 1973) 2, IAEA, Vienna (1974) 117

Ow60 : G.E. Owen and C.D. Swartz, Fast Neutr. Phys. Part 1. eds J.B. Marion and J.L. Fowler (Interscience, New York, 1960) 211

Pe40 : K.A. Petrzhak and G.N. Flerov, Sov. Phys. JETP 10 (1940) 1013

Pi78 : V.M. Piksaikin, P.P. D'yachenko, G.V. Ankin, E.A. Seregina, G.M. Akhmedov and V.S. Stavinskii, Sov. J. Nucl. Phys. 28 (1978) 314

Pr75 : J.S. Pringle and F.D. Brooks, Phys. Rev. Lett. 35 (1975) 1563

Pr77 : J.S. Pringle and F.D. Brooks, University of Cape Town, Physics Reports

Ra68 : G.M. Raisbeck and T.D. Thomas, Phys. Rev. 172 (1968) 1272

Sa65 : C.P. Sargent, W. Bertozzi, P.T. Demos, J.L. Matthews and W. Turchinetz, Phys. Rev. 137B (1965) 89

Sc83 : R. Schmitt and H. Henschel, Nucl. Phys. A395 (1983) 15

Sk63 : K. Skarsvag and K. Bergheim, Nucl. Phys. 45 (1963) 72

Sk70 : K. Skarsvag, Nucl. Phys. A153 (1970) 82

Sk73 : K. Skarsvag, Phys. Scr. 7 (1973) 160

Sk75 : K. Skarsvag, Nucl. Phys. A253 (1975) 274

Sp82 : R.R. Spencer, R. Gwin and R. Ingle, Nucl. Sci. Eng. 80 (1982) 603

St59 : V. Stavinskii, Sov. Phys. JETP 9 (1959) 437

St67 : V.M. Strutinsky, Nucl. Phys. A95 (1967) 420

St68 : V.M. Strutinsky, Nucl. Phys. A122 (1968) 7

Sw55 : W.J. Swiatecki, Phys. Rev. 100 (1955) 937

Ta75 : Tai No Han, A.H. Williams and G.H. McCall, Nucl. Instrum. Methods 131 (1975) 425

Te59 : J. Terrel, Phys. Rev. 113 (1959) 527

Te65 : J. Terrell, Phys. and Chem. of Fiss. (Proc. Symp. Salzburg 1965), 2 IAEA, Vienna (1965) 3

Th65 : T.D. Thomas, R.A. Atneosen, W,M Gibson and M.L. Perlman, Phys. and Chem. of Fiss. (Proc. Symp. Salzburg, 1965) 1 IAEA, Vienna (1965) 385

Wa52 : B.E. Watt, Phys. Rev. 87 (1952) 1037

Wa77 : R.L. Walsh and J.W. Boldeman, Nucl. Phys. A276 (1977) 189

We37 : V.F. Weisskopf, Phys. Rev. 52 (1937) 295

Wh63 : S.L. Whetstone, Phys. Rev 131 (1963) 1232

Wi47 : R.R. Wilson, Phys. Rev. 72 (1947) 189

Appendix A

The neutron detector measured an energy spectrum, N(E), where E is the energy of the neutron in the laboratory frame. This spectrum includes a correction for the variation of the detector efficiency with incident neutron energy, $\varepsilon(E)$, as outlined in sections 3.1 and 4.3.

For each event we determine the velocity, v, of the neutron in the laboratory frame, and the associated fragment velocity, V_F. From these quantities the velocity of the neutron in the restframe of the fragment, v_{PF}, is derived and hence the energy of the neutron in the restframe of the fragment, E_{PF}, is calculated. (These steps are summarised in the flow-diagram on page 4-16). An apparent (i.e. uncorrected) energy spectrum (e.g. figure 4.9(a)) of neutrons in the restframe of the fragment, $N'(E_{PF})$, can now be formed by suitable "binning" of the energy, E_{PF}, obtained for each event.

This is not a true representation of the neutron spectrum in the fragment restframe, however, because the effective solid angle, Ω_{EFF}, of the neutron detector in this frame depends on both v_{PF} and V_F.

To correct this distortion each event was weighted by a factor $\Phi(v_{PF},V_F)$, inversely proportional to the effective solid angle, Ω_{EFF}, and weights, rather than events, were summed in the energy bins represented by the final block in the flowchart (figure 4.8)

Consider an event in which the forward fragment has velocity V_F and the associated neutron that is detected has a velocity, v, in the laboratory frame. We distinguish the following limiting cases, shown in figure A.1 :

(1) the neutron is detected at the centre of the neutron detector. In this case v is the resultant of V_F and v_{PF}

(2) the neutron is detected at the edge of the detector, so that v is the resultant of V_F and v'_{PF}.

Now, in general, if $v \gg V_F$ then $v_{PF} \simeq v'_{PF}$. On the other hand, if $v \simeq V_F$ then $v'_{PF} >> v_{PF}$.

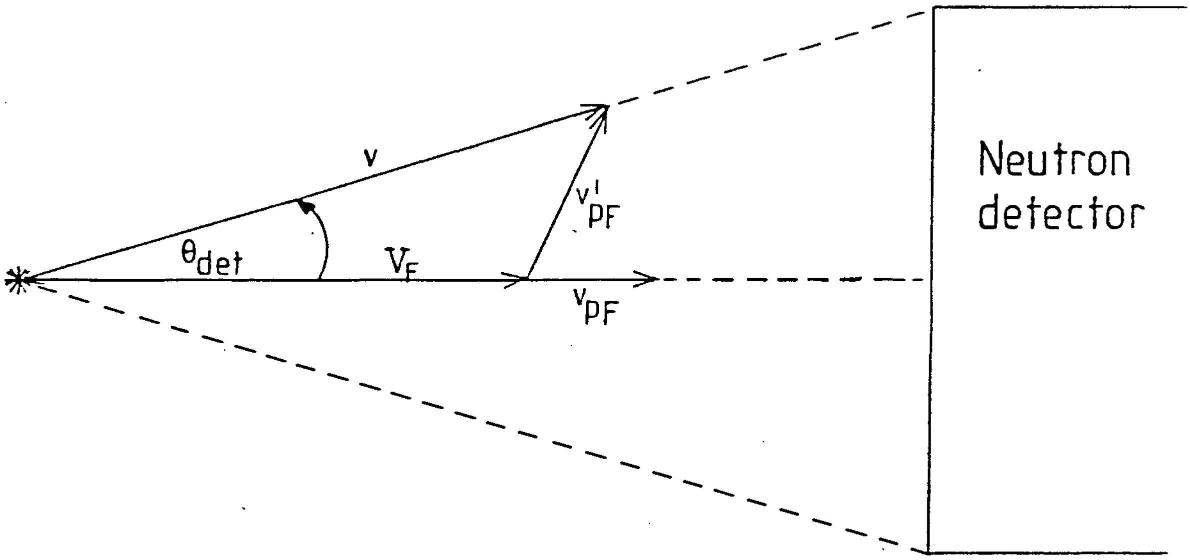

Figure A.1 Velocity vectors in the laboratory frame (V_F,v) and in the fragment restframe (v_{PF}, v'_{PF}).

In our case we note, firstly, that the angle Θ_{det} is small, viz. 6° and, secondly, that we reject events with $v \lesssim 1.2\ V_F$. The latter is a consequence of the fact that no data for the neutron energy spectrum in the restframe are presented below 0.1 MeV. The error that is introduced by assuming equal magnitudes for v_{PF} and v'_{PF} is estimated to be less than 12%. Using this approximation v_{PF} may thus be calculated from the experimental observations V_F and v for each event.

The factors (v_{PF}, V_F) were estimated by assuming isotropic emission of neutrons in the fragment restframe and determining the probability that the volocity combination of v_{PF} and V_F with v_{PF} randomly (see figure A.2) would lead to neutron emission in the direction of this detector.

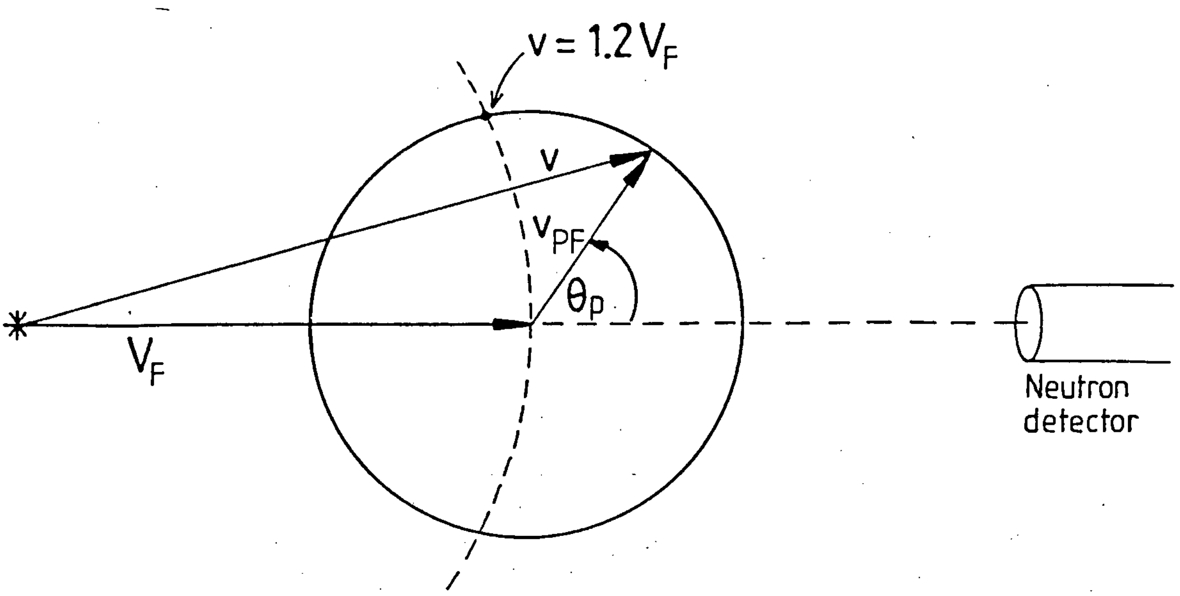

Figure A.2 The angle, ϴp, is changed in steps of 1° between 0° and 180° in the calculation of the kinematic factor Φ(v_{PF}, V_F). For a given pair of velocities, $\vec{v}_{PF}$ (direction random) and $\vec{V}_F$, (which points towards the neutron detector) only a fraction of the possible combinations give rise to laboratory neutron velocities, $\vec{v}$, directed within the cone of detection.

The angle, Θ_P, of the neutron in the fragment frame (see figure A.2) was varied in discrete steps $\Delta\Theta_P$ of 1° from $\Theta_P=0°$ to $\Theta_P=180°$. For the n^{th} step a weight, W_n, proportional to the number of neutrons emitted in all the directions (Θ_P,ϕ) where ϕ is integrated over 0° to 360°, is given by

$$W_n = \frac{2}{\Delta\Theta_P} \sin \left(\frac{2n+1}{2}\right) \Delta\Theta_P \qquad (A.2)$$

The factor Φ (v_{PF}, V_F) is then given by the ratio sums of weights:

$$\Phi\ (v_{PF},\ V_F) = \frac{\Sigma W_n'}{\Sigma W_n} \qquad (A.2)$$

where W_n' are the weights corresponding to the steps (angles) which satisfy the conditions

(i) $v > 1.2\ V_F$ (as imposed in the analysis) ; and

(ii) $\Theta_F < \Theta_{det}$ (required for the neutron to pass through the detector)

A matrix of values was calculated for v_{PF} and V_F ranging over values appropriate to the experimental data. These values formed a reference table from which Φ-values were read event-by-event for the calculation of neutron spectra (e.g. figure 4.9(b)) in the fragment restframe.